1

Remote Observations of the Main Belt

PIERRE VERNAZZA, FUMIHIKO USUI, AND SUNAO HASEGAWA

1.1 INTRODUCTION

It might be no exaggeration to say that the history of asteroid science has always been driven by the history of research on the largest Main Belt asteroids (with diameters greater than ∼100 km), with Ceres and Vesta being the most studied bodies. Because of their brightness and scientific interest due to their large size (between that of the most common asteroids and planets), the largest asteroids have always been privileged targets for every new generation telescope and/or instrument. Today, the asteroid belt contains ∼230 such bodies (see Table 1.1 for a complete list of D ≳200 km bodies and Table 1.2 for a complete list of D ≳100 km bodies). Spectrophotometric observations have been carried out for all of these bodies in the visible and/or near-infrared range. Among the 25 spectral types defined within the Bus-DeMeo asteroid taxonomy based on principal components analysis of combined visible and near-infrared spectral data spanning wavelengths from 0.45 to 2.45 μm for nearly 400 asteroids (DeMeo et al., 2009), only O-, Q-, and Xn-type asteroids are absent among D > 100 km bodies. C-complex asteroids (B, C, Cb, Cg, Cgh, Ch), S-complex asteroids (Q, S, Sa, Sq, Sr, Sv), P/D type asteroids (low albedo X, T, and D-types), and the remaining types (1 A-type, 4 K-type, 2 L-type, 1 R-type, 1 V-type, 1 high albedo X-type, 2 Xe-type, 9 Xc-type, 15 Xk-type) represent, respectively, 61%, 10%, 13%, and 16% of all D > 100 km asteroids.

Early photometric observations of these bodies were key in establishing the existence of a compositional gradient in the asteroid belt (Gradie & Tedesco, 1982), with S-types being located on average closer to the Sun than C-types and P-/D-types being the farthest from the Sun. On the basis of these observations, scenarios regarding the formation and dynamical evolution of the asteroid belt and that of the Solar System in general have been formulated (e.g., Gomes et al., 2005; Morbidelli et al., 2005; Tsiganis et al., 2005; Bottke et al., 2006; Levison et al., 2009; Walsh et al., 2011; Raymond & Izidoro, 2017). These dynamical models suggest that today's asteroid belt may not only host objects that formed in situ, typically between 2.2 and 3.3 AU, but also bodies that were formed in the terrestrial planet region (Xe- and possibly S-types), in the giant planet region (Ch/Cgh- and B/C-types) as well as beyond Neptune (P/D-types). In a broad stroke, the idea that the asteroid belt is a condensed version of the primordial Solar System has progressively emerged. Notably, these observations along with those of more distant small bodies (giant planet trojans, trans-Neptunian objects) were instrumental in imposing giant planet migrations as a main step in the dynamical evolution of our Solar System. On the basis of these datasets, the idea of a static Solar System history has dramatically shifted to one of dynamic change and mixing (DeMeo & Carry, 2014). See Part III of this book for more details on this topic.

The study of the largest Main Belt asteroids is not only important because of the clues it delivers regarding the formation and evolution of the belt itself but also because many of these bodies are likely "primordial" remnants of the early Solar System (Morbidelli et al., 2009), that is their internal structure has likely remained intact since their formation (they can be seen as the smallest protoplanets). Many of these bodies thus offer, similarly to Ceres and Vesta detailed in the present book, invaluable constraints regarding the processes of protoplanet formation over a wide range of heliocentric distances (assuming that the aforementioned migration theories are correct).

In the present chapter, we review the current knowledge regarding large (D ≳100 km) Main Belt asteroids derived from Earth-based spectroscopic and imaging observations with an emphasis on D > 200 km bodies including Ceres and Vesta. Our motivation is to provide a meaningful context for the two largest Main Belt asteroids visited by the Dawn mission (see Chapter 2) and to guide future in-situ investigations to the largest asteroids – that's why small (D < 100 km) asteroids, which are essentially the leftover fragments of catastrophic collisions, are not discussed here.

1.2 SPECTROSCOPIC OBSERVATIONS OF LARGE MAIN BELT ASTEROIDS

Detailed reviews concerning the compositional interpretation of asteroid taxonomic types and their distribution across the Main Belt can be found in Burbine (2014, 2016), DeMeo et al. (2015), Reddy et al. (2015), Vernazza et al. (2015b), Vernazza and Beck (2017), and Greenwood et al. (2020) and will not be repeated with the same level of detail in this chapter. Rather, we put the emphasis on the currently proposed connections between the various compositional classes present among the largest Main Belt asteroids and the two main classes of extra-terrestrial materials, namely meteorites and interplanetary dust particles (hereafter IDPs). The two largest asteroids, Vesta and Ceres, "heroes" of the present book, illustrate well the Main Belt paradox: some asteroids appear well sampled by meteorites (Vesta) whereas others don't (Ceres). IDPs may be more appropriate analogues

FU was supported by JSPS KAKENHI: grant nos. JP19H00725, JP20H00188, and JP20K04055. SH was supported by JSPS KAKENHI (grant nos. JP15K05277, JP17K05636, JP18K03723, JP19H00719, and JP20K04055) and by the Hypervelocity Impact Facility (former facility name: the Space Plasma Laboratory), ISAS, JAXA.

Table 1.1 *Volume equivalent diameter (Deq), geometric albedo, spectral type following the Bus-DeMeo taxonomy, semi-major axis (a), eccentricity (e), and inclination (i) for the largest (D > 200 km) Main Belt asteroids listed according to decreasing values of their size.*

The albedo and diameter values represent the averages of the values reported in Tedesco et al. (2002), Usui et al. (2011), and Masiero et al. (2011, 2014). Spectral types were retrieved from Bus and Binzel (2002), Lazzaro et al. (2004), and DeMeo et al. (2009)

Object	Deq (km)	Geom. alb.	Spectral type	a (AU)	e	i (deg)
1 Ceres	939.4	0.087	C	2.77	0.08	10.59
4 Vesta	525.4	0.404	V	2.36	0.09	7.14
2 Pallas	513.0	0.140	B	2.77	0.23	34.83
10 Hygiea	434.0	0.059	C	3.14	0.11	3.83
704 Interamnia	332.0	0.044	Cb	3.06	0.16	17.31
52 Europa	314.0	0.049	C	3.09	0.11	7.48
511 Davida	303.2	0.064	C	3.16	0.19	15.94
65 Cybele	286.3	0.049	Xk	3.42	0.11	3.56
87 Sylvia	280.0	0.043	X	3.48	0.09	10.88
31 Euphrosyne	268.0	0.047	Cb	3.16	0.22	26.28
15 Eunomia	267.3	0.196	S	2.64	0.19	11.75
107 Camilla	254.0	0.040	X	3.49	0.07	10.00
3 Juno	249.0	0.210	Sq	2.67	0.26	12.99
451 Patientia	242.9	0.069	C	3.06	0.07	15.24
324 Bamberga	232.9	0.061	C	2.68	0.34	11.10
16 Psyche	222.0	0.156	Xk	2.92	0.13	3.10
48 Doris	220.8	0.064	Ch	3.11	0.07	6.55
88 Thisbe	212.0	0.052	C	2.77	0.16	5.21
423 Diotima	211.2	0.053	C	3.07	0.04	11.24
19 Fortuna	211.0	0.048	Ch	2.44	0.16	1.57
13 Egeria	205.0	0.080	Ch	2.58	0.09	16.54
7 Iris	204.0	0.244	S	2.39	0.23	5.52
29 Amphitrite	204.0	0.185	S	2.55	0.07	6.08

for these bodies. We first start by summarizing the results of Earth-based spectroscopic campaigns devoted to constrain the surface composition of Ceres and Vesta and then continue by summarizing current knowledge regarding the surface composition of D > 100 km asteroids.

1.2.1 Focus on Earth-based Spectroscopic Observations of Ceres and Vesta and Comparison to Dawn Measurements

1.2.1.1 (1) Ceres

In the 1970s, Ceres was identified as a carbonaceous chondrite-like asteroid based on a low albedo (~0.05–0.06) (Veverka, 1970; Matson, 1971; Bowell & Zellner, 1973) and a relatively flat reflectance from 0.5 to 2.5 μm (Chapman et al., 1973, 1975; Johnson & Fanale, 1973; Johnson et al., 1975). A few years later, a ~3.1 μm absorption feature was discovered in its spectrum (Lebofsky, 1978; Lebofsky et al., 1981) and was interpreted as indicative of the presence of hydrated clay minerals similar to those present in carbonaceous chondrites at the surface of Ceres. Subsequent work proposed ammoniated saponite (King et al., 1992) and water ice (Vernazza et al., 2005) as the origin of this band. The presence of water ice in the subsurface of Ceres was predicted based on the detection of OH escaping from the north polar region (A'Hearn & Feldman, 1992). Rivkin et al. (2006b) reported the presence of carbonates and iron-rich clays at the surface of Ceres based on spectroscopic measurements in the 2–4 μm range. This compositional interpretation was refined a few years later (Milliken & Rivkin, 2009) and an assemblage consisting of a mixture of hydroxide brucite, magnesium carbonates, and serpentines was proposed to explain Ceres' spectral properties. Recent observations with the AKARI satellite have revealed the presence of an additional absorption band in the 2.5–3.5 μm range that is located at 2.73 μm (Usui et al., 2019), while also confirming the presence of a band at 3.06–3.08 μm (Usui et al., 2019). Measurements performed by the VIR instrument onboard the Dawn mission have shown that the ~3.06 μm band assigned to ammoniated phyllosilicates by King et al. (1992) is the most

https://doi.org/10.1017/9781108856324.003 Published online by Cambridge University Press

Table 1.2 *Volume equivalent diameter (Deq), geometric albedo, spectral type following the Bus-DeMeo taxonomy, semi-major axis (a), eccentricity (e), and inclination (i) for the largest (D > 100 km) Main Belt asteroids.*

The albedo and diameter values represent the averages of the values reported in Tedesco et al. (2002), Masiero et al. (2011, 2014), and Usui et al. (2011). Spectral types were retrieved from Bus and Binzel (2002), Lazzaro et al. (2004), and DeMeo et al. (2009). The spectral type in braces was determined using the Bus and Binzel (2002) taxonomy

Object	Deq (km)	Geom. Alb.	Spectral type	a (AU)	e	i (deg)
1 Ceres	939.4	0.087	C	2.77	0.08	10.59
2 Pallas	513.0	0.140	B	2.77	0.23	34.83
3 Juno	249.0	0.210	Sq	2.67	0.26	12.99
4 Vesta	525.4	0.404	V	2.36	0.09	7.14
5 Astraea	114.0	0.236	S	2.57	0.19	5.37
6 Hebe	196.0	0.220	S	2.43	0.20	14.75
7 Iris	204.0	0.244	S	2.39	0.23	5.52
8 Flora	140.0	0.226	Sw	2.20	0.16	5.89
9 Metis	168.0	0.189	K	2.39	0.12	5.58
10 Hygiea	434.0	0.059	C	3.14	0.11	3.83
11 Parthenope	154.5	0.186	Sq	2.45	0.10	4.63
12 Victoria	129.7	0.134	L	2.33	0.22	8.37
13 Egeria	205.0	0.080	Ch	2.58	0.09	16.54
14 Irene	149.7	0.239	S	2.59	0.17	9.12
15 Eunomia	267.3	0.196	S	2.64	0.19	11.75
16 Psyche	222.0	0.156	Xk	2.92	0.13	3.10
18 Melpomene	146.0	0.190	S	2.30	0.22	10.13
19 Fortuna	211.0	0.048	Ch	2.44	0.16	1.57
20 Massalia	140.8	0.229	S	2.41	0.14	0.71
21 Lutetia	98.0	0.184	Xc	2.44	0.16	3.06
22 Kalliope	161.0	0.171	X	2.91	0.10	13.72
23 Thalia	105.1	0.270	S	2.63	0.24	10.11
24 Themis	189.6	0.074	C	3.14	0.13	0.75
27 Euterpe	113.9	0.218	S	2.35	0.17	1.58
28 Bellona	122.7	0.187	S	2.78	0.15	9.43
29 Amphitrite	204.0	0.185	S	2.55	0.07	6.08
31 Euphrosyne	268.0	0.047	Cb	3.16	0.22	26.28
34 Circe	117.1	0.051	Ch	2.69	0.10	5.50
35 Leukothea	104.1	0.066	(C)	2.99	0.23	7.94
36 Atalante	111.5	0.060	Ch	2.75	0.30	18.43
37 Fides	110.0	0.182	S	2.64	0.17	3.07
38 Leda	116.1	0.063	Cgh	2.74	0.15	6.97
39 Laetitia	164.0	0.238	Sqw	2.77	0.11	10.38
40 Harmonia	116.7	0.209	S	2.27	0.05	4.26
41 Daphne	187.0	0.055	Ch	2.76	0.28	15.79
42 Isis	106.7	0.152	K	2.44	0.22	8.53
45 Eugenia	186.0	0.051	C	2.72	0.08	6.60
46 Hestia	126.0	0.051	Xc	2.53	0.17	2.34
47 Aglaja	142.0	0.064	C	2.88	0.13	4.98

https://doi.org/10.1017/9781108856324.003 Published online by Cambridge University Press

Table 1.2 (*cont.*)

Object	Deq (km)	Geom. Alb.	Spectral type	a (AU)	e	i (deg)
48 Doris	220.8	0.064	Ch	3.11	0.07	6.55
49 Pales	161.3	0.052	Ch	3.09	0.23	3.17
50 Virginia	94.4	0.041	Ch	2.65	0.28	2.83
51 Nemausa	144.0	0.078	Cgh	2.37	0.07	9.98
52 Europa	314.0	0.049	C	3.09	0.11	7.48
53 Kalypso	110.7	0.044	Ch	2.62	0.21	5.17
54 Alexandra	143.0	0.066	Cgh	2.71	0.20	11.80
56 Melete	120.0	0.060	Xk	2.60	0.24	8.07
57 Mnemosyne	114.5	0.209	S	3.15	0.12	15.22
59 Elpis	168.0	0.043	C	2.71	0.12	8.63
62 Erato	97.0	0.063	B	3.13	0.17	2.23
65 Cybele	286.3	0.049	Xk	3.43	0.11	3.56
68 Leto	127.2	0.215	S	2.78	0.19	7.97
69 Hesperia	134.8	0.150	Xk	2.98	0.17	8.59
70 Panopaea	137.1	0.050	Cgh	2.61	0.18	11.59
74 Galatea	122.6	0.042	(C)	2.78	0.24	4.08
76 Freia	173.1	0.042	C	3.41	0.16	2.12
78 Diana	145.5	0.051	Ch	2.62	0.21	8.70
81 Terpsichore	124.0	0.042	C	2.86	0.21	7.80
85 Io	165.0	0.054	C	2.66	0.19	11.96
86 Semele	119.2	0.049	Cgh	3.11	0.21	4.82
87 Sylvia	280.0	0.043	X	3.48	0.09	10.88
88 Thisbe	212.0	0.052	C	2.77	0.16	5.21
89 Julia	140.0	0.172	S	2.55	0.18	16.14
90 Antiope	108.0	0.087	C	3.16	0.16	2.21
91 Aegina	109.0	0.042	Ch	2.59	0.11	2.11
92 Undina	121.0	0.280	Xk	3.19	0.10	9.93
93 Minerva	159.0	0.048	C	2.76	0.14	8.56
94 Aurora	199.0	0.041	C	3.16	0.09	7.97
95 Arethusa	144.5	0.062	Ch	3.07	0.15	13.00
96 Aegle	172.9	0.051	T	3.05	0.14	15.97
98 Ianthe	109.8	0.043	(Ch)	2.69	0.19	15.58
104 Klymene	127.8	0.054	Ch	3.15	0.16	2.79
105 Artemis	121.0	0.045	Ch	2.37	0.18	21.44
106 Dione	174.7	0.067	Cgh	3.18	0.17	4.60
107 Camilla	254.0	0.040	X	3.49	0.07	10.00
111 Ate	144.9	0.053	Ch	2.59	0.10	4.93
114 Kassandra	99.0	0.090	K	2.68	0.14	4.93
117 Lomia	158.6	0.048	(X)	2.99	0.03	14.90
120 Lachesis	170.2	0.050	C	3.12	0.06	6.95
121 Hermione	187.0	0.061	Ch	3.45	0.13	7.60
127 Johanna	121.7	0.053	Ch	2.76	0.07	8.24

https://doi.org/10.1017/9781108856324.003 Published online by Cambridge University Press

Table 1.2 (*cont.*)

Object	Deq (km)	Geom. Alb.	Spectral type	a (AU)	e	i (deg)
128 Nemesis	185.4	0.053	C	2.75	0.12	6.25
129 Antigone	126.0	0.147	Xk	2.88	0.21	12.23
130 Elektra	199.0	0.064	Ch	3.12	0.21	22.86
134 Sophrosyne	113.3	0.045	(Ch)	2.56	0.12	11.60
137 Meliboea	147.8	0.049	(C)	3.12	0.22	13.41
139 Juewa	167.2	0.047	(X)	2.78	0.18	10.91
140 Siwa	114.0	0.063	Xc	2.73	0.22	3.19
141 Lumen	136.4	0.050	Ch	2.67	0.21	11.89
144 Vibilia	141.0	0.051	Ch	2.66	0.24	4.81
145 Adeona	150.1	0.044	Ch	2.67	0.15	12.64
146 Lucina	134.5	0.052	Ch	2.72	0.07	13.10
147 Protogeneia	121.8	0.062	C	3.14	0.03	1.93
150 Nuwa	145.5	0.043	C	2.98	0.13	2.19
153 Hilda	186.6	0.055	X	3.97	0.14	7.83
154 Bertha	187.0	0.047	(C)	3.20	0.08	20.98
156 Xanthippe	113.6	0.048	Ch	2.73	0.23	9.78
159 Aemilia	130.0	0.059	Ch	3.10	0.11	6.13
162 Laurentia	98.6	0.055	(Ch)	3.02	0.18	6.10
164 Eva	107.7	0.039	(X)	2.63	0.34	24.47
165 Loreley	173.0	0.045	(Cb)	3.12	0.08	11.22
168 Sibylla	148.8	0.054	(Ch)	3.37	0.07	4.64
171 Ophelia	110.6	0.071	(Cb)	3.13	0.13	2.55
173 Ino	152.6	0.069	Xk	2.74	0.21	14.21
175 Andromache	110.8	0.071	Cg	3.18	0.23	3.22
176 Iduna	124.3	0.080	(Ch)	3.19	0.17	22.59
181 Eucharis	118.2	0.095	Xk	3.13	0.20	18.89
185 Eunike	168.2	0.057	C	2.74	0.13	23.22
187 Lamberta	131.8	0.059	Ch	2.73	0.24	10.59
190 Ismene	197.3	0.043	X	4.00	0.17	6.16
191 Kolga	102.3	0.040	Cb	2.89	0.09	11.51
194 Prokne	172.6	0.050	Ch	2.62	0.24	18.49
196 Philomela	148.8	0.195	(S)	3.11	0.02	7.26
200 Dynamene	133.4	0.050	(Ch)	2.74	0.13	6.90
203 Pompeja	111.3	0.045	(C-complex)	2.74	0.06	3.18
206 Hersilia	99.3	0.062	(C)	2.74	0.04	3.78
209 Dido	138.2	0.049	(Xc)	3.14	0.06	7.17
210 Isabella	85.8	0.048	Cb	2.72	0.12	5.26
211 Isolda	149.2	0.056	Ch	3.04	0.16	3.89
212 Medea	150.0	0.039	X	3.12	0.11	4.26
216 Kleopatra	121.0	0.145	Xe	2.80	0.25	13.10
221 Eos	105.6	0.139	K	3.01	0.10	10.88
225 Henrietta	119.3	0.042	(B)	3.39	0.26	20.87

https://doi.org/10.1017/9781108856324.003 Published online by Cambridge University Press

Table 1.2 (*cont.*)

Object	Deq (km)	Geom. Alb.	Spectral type	a (AU)	e	i (deg)
227 Philosophia	97.6	0.056	(X)	3.17	0.19	9.11
229 Adelinda	104.2	0.037	X	3.42	0.14	2.08
230 Athamantis	112.0	0.163	S	2.38	0.06	9.44
233 Asterope	106.0	0.157	Xk	2.66	0.10	7.69
238 Hypatia	151.4	0.042	(Ch)	2.91	0.09	12.39
241 Germania	178.7	0.052	C	3.05	0.10	5.51
247 Eukrate	147.0	0.051	(Xc)	2.74	0.24	24.99
250 Bettina	111.0	0.137	Xk	3.15	0.13	12.81
259 Aletheia	185.3	0.041	(X)	3.13	0.13	10.82
266 Aline	112.1	0.048	Ch	2.80	0.16	13.40
268 Adorea	148.9	0.040	X	3.09	0.14	2.44
275 Sapientia	110.9	0.042	C	2.77	0.16	4.76
276 Adelheid	123.9	0.046	X	3.12	0.07	21.62
279 Thule	124.9	0.043	D	4.28	0.01	2.34
283 Emma	142.0	0.032	C	3.05	0.15	7.99
286 Iclea	103.9	0.043	(Ch)	3.19	0.03	17.90
303 Josephina	103.4	0.052	(Ch)	3.12	0.06	6.87
308 Polyxo	147.3	0.045	T	2.75	0.04	4.36
324 Bamberga	232.9	0.061	C	2.68	0.34	11.10
328 Gudrun	120.1	0.045	C/Cb	3.11	0.11	16.12
334 Chicago	182.7	0.050	C	3.90	0.02	4.64
344 Desiderata	133.9	0.058	Xk	2.60	0.32	18.35
345 Tercidina	101.5	0.058	Ch	2.33	0.06	9.75
349 Dembowska	174.4	0.280	R	2.93	0.09	8.25
350 Ornamenta	114.3	0.063	(Ch)	3.11	0.16	24.91
354 Eleonora	159.9	0.187	A	2.80	0.12	18.40
356 Liguria	134.2	0.051	Ch	2.76	0.24	8.22
357 Ninina	104.6	0.053	(B)	3.15	0.07	15.08
360 Carlova	135.0	0.039	(C)	3.00	0.18	11.70
361 Bononia	150.5	0.041	D	3.96	0.21	12.62
365 Corduba	101.6	0.037	(C)	2.80	0.16	12.78
372 Palma	192.6	0.064	(B)	3.15	0.26	23.83
373 Melusina	98.7	0.042	(Ch)	3.12	0.14	15.43
375 Ursula	193.6	0.049	C	3.12	0.11	15.94
381 Myrrha	127.6	0.055	(Cb)	3.22	0.09	12.53
386 Siegena	167.0	0.053	(C)	2.90	0.17	20.26
387 Aquitania	97.0	0.171	L	2.74	0.24	18.13
388 Charybdis	122.2	0.044	(C)	3.01	0.06	6.44
393 Lampetia	121.9	0.064	(Xc)	2.78	0.33	14.88
404 Arsinoe	98.0	0.047	(Ch)	2.59	0.20	14.11
405 Thia	124.4	0.048	Ch	2.58	0.24	11.95
409 Aspasia	164.0	0.060	Xc	2.58	0.07	11.26

https://doi.org/10.1017/9781108856324.003 Published online by Cambridge University Press

Table 1.2 (*cont.*)

Object	Deq (km)	Geom. Alb.	Spectral type	a (AU)	e	i (deg)
410 Chloris	116.6	0.058	(Ch)	2.73	0.24	10.96
412 Elisabetha	100.6	0.043	(C)	2.76	0.04	13.78
419 Aurelia	122.5	0.043	C	2.60	0.25	3.93
420 Bertholda	148.7	0.038	D	3.41	0.03	6.69
423 Diotima	211.2	0.053	C	3.07	0.04	11.24
426 Hippo	123.0	0.051	B	2.89	0.10	19.48
444 Gyptis	165.6	0.047	C	2.77	0.18	10.28
445 Edna	97.6	0.037	(Ch)	3.20	0.19	21.38
451 Patientia	242.9	0.069	C	3.06	0.07	15.24
455 Bruchsalia	98.5	0.052	(Xk)	2.66	0.29	12.02
466 Tisiphone	111.0	0.072	(Ch)	3.35	0.09	19.11
469 Argentina	127.4	0.039	(Xk)	3.18	0.16	11.59
471 Papagena	132.0	0.232	Sq	2.89	0.23	14.98
476 Hedwig	124.5	0.045	Xk	2.65	0.07	10.94
481 Emita	112.5	0.047	(Ch)	2.74	0.16	9.84
488 Kreusa	161.4	0.052	(Ch)	3.17	0.16	11.52
489 Comacina	138.8	0.044	(X)	3.15	0.04	13.00
490 Veritas	114.5	0.064	Ch	3.17	0.10	9.28
491 Carina	99.1	0.063	(C)	3.19	0.09	18.87
505 Cava	102.8	0.060	Xk	2.68	0.25	9.84
506 Marion	108.0	0.045	(X)	3.04	0.15	17.00
508 Princetonia	134.9	0.050	(X)	3.16	0.01	13.36
511 Davida	303.2	0.064	C	3.16	0.19	15.94
514 Armida	105.6	0.040	(Xe)	3.05	0.04	3.88
517 Edith	96.3	0.037	C	3.16	0.18	3.19
521 Brixia	118.9	0.060	Ch	2.74	0.28	10.60
522 Helga	97.2	0.044	(X)	3.63	0.08	4.44
532 Herculina	191.0	0.211	S	2.77	0.18	16.31
536 Merapi	159.5	0.042	Xk	3.50	0.09	19.43
545 Messalina	112.2	0.042	(Cb)	3.21	0.17	11.12
554 Peraga	102.9	0.039	Ch	2.38	0.15	2.94
566 Stereoskopia	167.0	0.042	(X)	3.38	0.11	4.90
570 Kythera	102.4	0.051	D	3.42	0.12	1.79
595 Polyxena	110.6	0.091	(T)	3.21	0.06	17.82
596 Scheila	114.3	0.038	T	2.93	0.16	14.66
602 Marianna	128.9	0.051	(Ch)	3.09	0.25	15.08
618 Elfriede	133.6	0.050	(C)	3.19	0.07	17.04
635 Vundtia	99.0	0.045	(B)	3.14	0.08	11.03
654 Zelinda	128.3	0.042	(Ch)	2.30	0.23	18.13
683 Lanzia	103.0	0.108	(C)	3.12	0.06	18.51
690 Wratislavia	157.9	0.044	(B)	3.14	0.18	11.27
694 Ekard	105.3	0.037	(Ch)	2.67	ign="left">0.32	15.84

https://doi.org/10.1017/9781108856324.003 Published online by Cambridge University Press

Table 1.2 (*cont.*)

Object	Deq (km)	Geom. Alb.	Spectral type	a (AU)	e	i (deg)
702 Alauda	195.0	0.056	C	3.19	0.02	20.61
704 Interamnia	332.0	0.044	Cb	3.06	0.16	17.31
705 Erminia	137.4	0.042	(C)	2.92	0.05	25.04
712 Boliviana	127.4	0.049	(X)	2.58	0.19	12.76
713 Luscinia	101.8	0.044	(C)	3.39	0.17	10.36
733 Mocia	102.6	0.041	(X)	3.40	0.06	20.26
739 Mandeville	111.2	0.054	Xc	2.74	0.14	20.66
747 Winchester	178.0	0.048	(C)	3.00	0.34	18.16
748 Simeisa	106.6	0.039	(T)	3.96	0.19	2.26
751 Faina	111.9	0.050	(Ch)	2.55	0.15	15.61
762 Pulcova	149.0	0.055	C	3.16	0.10	13.09
769 Tatjana	106.3	0.044	(C-complex)	3.17	0.19	7.37
772 Tanete	130.6	0.050	C	3.00	0.09	28.86
776 Berbericia	155.6	0.063	Cgh	2.93	0.16	18.25
780 Armenia	99.7	0.045	(C)	3.11	0.10	19.09
786 Bredichina	101.3	0.060	(X/Xc)	3.17	0.16	14.55
788 Hohensteina	119.2	0.060	(Ch)	3.12	0.13	14.34
790 Pretoria	159.1	0.045	(X)	3.41	0.15	20.53
804 Hispania	158.8	0.052	(C)	2.84	0.14	15.36
814 Tauris	111.0	0.045	(C)	3.15	0.31	21.83
895 Helio	134.2	0.049	(B)	3.20	0.15	26.09
909 Ulla	114.8	0.036	X	3.54	0.09	18.79
1015 Christa	100.6	0.043	(Xc)	3.21	0.08	9.46
1021 Flammario	101.0	0.045	C	2.74	0.28	15.87
1093 Freda	112.2	0.043	(Cb)	3.13	0.27	25.21
1269 Rollandia	108.2	0.045	(D)	3.91	0.10	2.76

plausible interpretation (De Sanctis et al., 2015), while the assemblage with brucite was not confirmed. The VIR instrument has further revealed the presence of water ice (Combe et al., 2016), carbonates (De Sanctis et al., 2016), organics (De Sanctis et al., 2017), and chloride salts (De Sanctis et al., 2020) at the surface of Ceres. See Chapters 7 and 8 for more detail.

Notably, a "genetic" link between Ceres and carbonaceous chondrites available in our collections has progressively been questioned with time (Milliken & Rivkin, 2009; Rivkin et al., 2011). First, the ∼3.06 μm band present in Ceres spectrum differs from what is seen in carbonaceous chondrite spectra. Second, the band depth of the 2.73 μm band is shallower than that of CM-like (Ch-/Cgh-type) asteroids (Figure 1.1; Usui et al., 2019). Third, Ceres' spectrum possesses a broad absorption band centered on ∼1.2–1.3 μm that is not seen in spectra of aqueously altered carbonaceous chondrite (Figure 1.1). Vernazza et al. (2015a) and Marsset et al. (2016) have tentatively attributed this absorption band to amorphous silicates (mainly olivine), whereas Yang and Jewitt (2010) proposed magnetite instead. Observations in the mid-infrared wavelength range have further reinforced the existence of compositional differences between Ceres and carbonaceous chondrite meteorites (Vernazza et al., 2017, Figure 1.2). They have further revealed the presence of anhydrous silicates at the surface of Ceres in addition to phyllosilicates and carbonates.

1.2.1.2 (4) Vesta

It has been well known since the 1970s that Vesta possesses a high albedo (0.3–0.4) (e.g., Allen, 1970; Cruikshank & Morrison, 1973; Tedesco et al., 2002; Ryan & Woodward, 2010; Usui et al., 2011; Hasegawa et al., 2014) and that its surface is basaltic in composition (McCord et al., 1970; Larson & Fink, 1975; McFadden et al., 1977). Vesta's spectrum displays two diagnostic absorption bands centered at ∼0.9 μm and ∼2 μm which imply the presence of pyroxene at its surface. A comparison of these observations with laboratory measurements of meteorites has revealed a spectral similarity between Vesta and that of the howardite–eucrite–diogenite (HED) achondritic meteorites (e.g., McCord et al., 1970; Feierberg & Drake, 1980; Feierberg et al., 1980;

https://doi.org/10.1017/9781108856324.003 Published online by Cambridge University Press

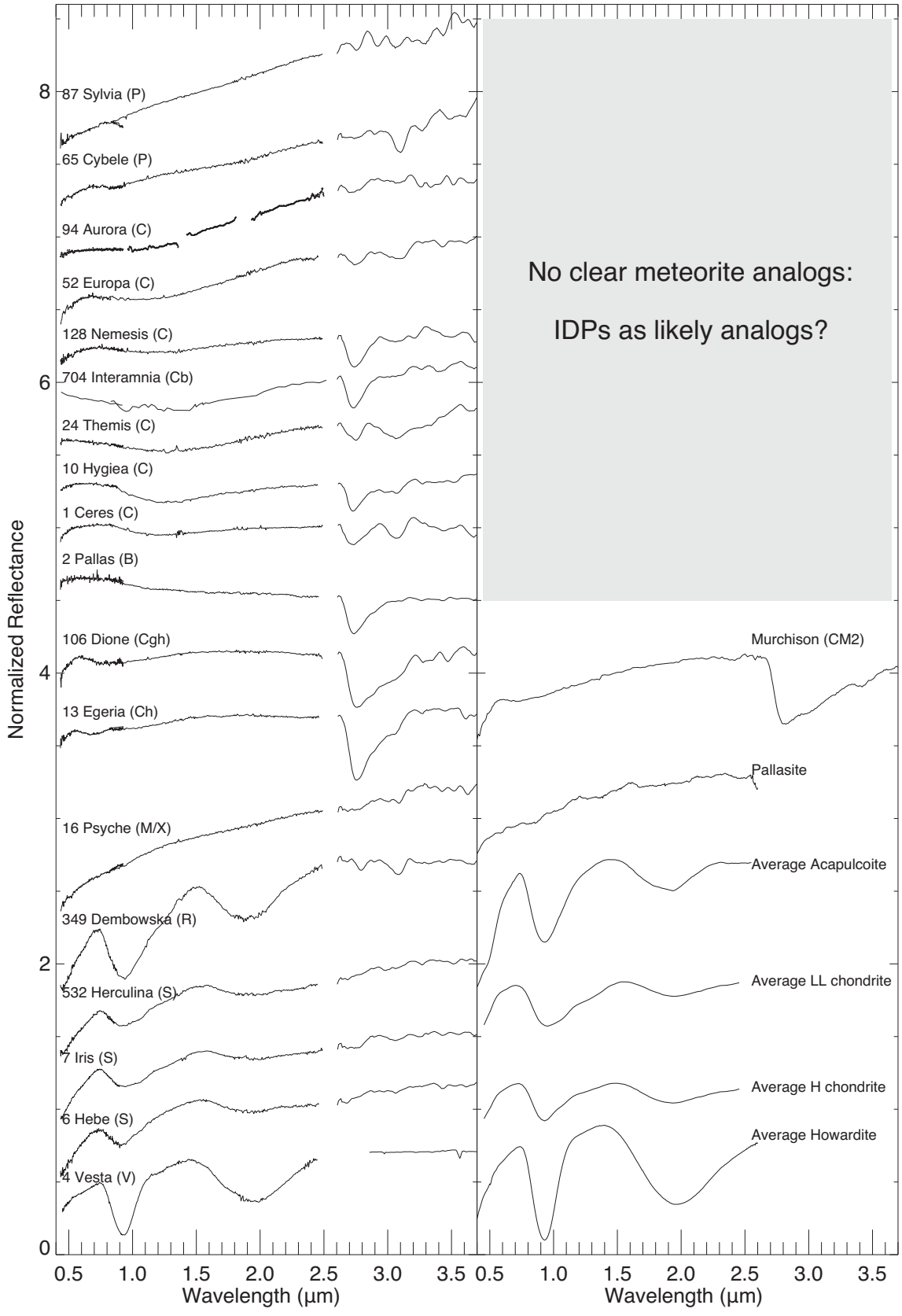

Figure 1.1 Sample of reflectance spectra of D > 100 km asteroids in visible to near-infrared wavelengths obtained with ground-based telescopes (Bus & Binzel, 2002; Hasegawa et al., 2003, 2017; Hardersen et al., 2004; Lazzaro et al., 2004; Rivkin et al., 2006a; DeMeo et al., 2009; Vernazza et al., 2014; Binzel et al., 2019; some spectra were also retrieved from the smass.mit.edu database) and the AKARI satellite (Usui et al., 2019) representative of the compositional diversity among these bodies. The asteroid spectral types are indicated in parentheses. Spectra of analogue meteorites are also shown next to each asteroid type (data are retrieved from the RELAB spectral database). The gray region denotes the asteroid types for which no clear meteoritic analogues exist.

https://doi.org/10.1017/9781108856324.003 Published online by Cambridge University Press

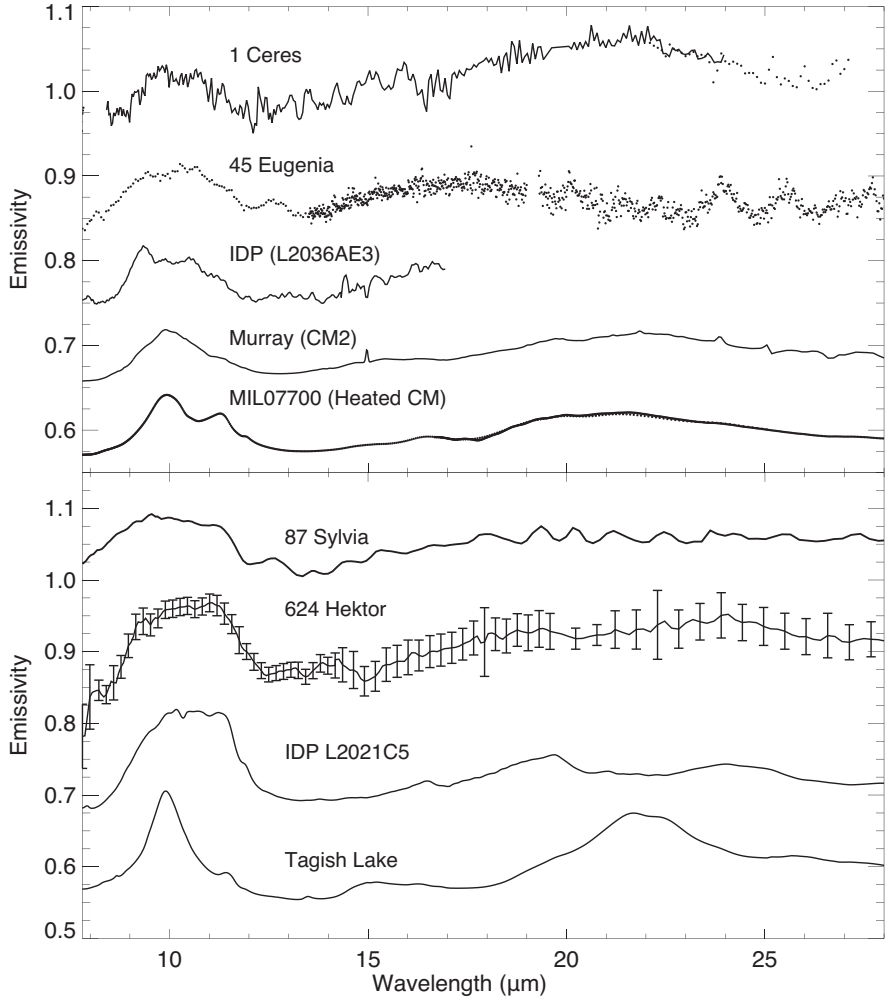

Figure 1.2 Emissivity spectra of C- (top) and P/D-type asteroids (bottom) compared to meteorite and IDP spectra. The data were retrieved from Emery et al. (2006), Brunetto et al. (2011), Marchis et al. (2012), Merouane et al. (2014), and Vernazza et al. (2017). Here, we illustrate the typical mismatch between carbonaceous chondrites and most C-, P-, and D-type asteroids (Vernazza et al., 2015a). IDPs instead appear as more convincing analogues for these objects.

Hiroi et al., 1994), opening the possibility that Vesta could be the parent body of this meteorite group (e.g., Drake, 2001). Spectroscopic observations in the 3-μm region have delivered contrasting results. Hasegawa et al. (2003) were the first to report the presence of a shallow 3-μm absorption that they interpreted either as contamination by CM-like impactors or solar wind implantation. These results were not confirmed by Vernazza et al. (2005), whereas Rivkin et al. (2006a) could not formally rule out a shallow (∼1%) absorption band. Finally, the presence of olivine has been reported at the surface of Vesta on the basis of spectral and color data (Binzel et al., 1997; Gaffey, 1997; Dotto et al., 2000; Heras et al., 2000).

The heterogeneity of Vesta's surface composition has been studied since the late 1970s (e.g., Blanco & Catalano, 1979; Degewij et al., 1979; Binzel et al., 1997; Gaffey, 1997; Vernazza et al., 2005; Rivkin et al., 2006a; Carry et al., 2010c), revealing a non-uniform surface composition which was later confirmed by the data obtained by the Dawn spacecraft's visible and infrared spectrometer (De Sanctis et al., 2012). The Dawn measurements have further confirmed that the mineralogy of Vesta is consistent with HED meteorites while also revealing the presence of olivine-rich areas in unexpected locations far from the Rheasilvia impact basin (Ammannito et al., 2013). For a detailed discussion see Chapter 3.

The primordial Vesta material is no longer found on Vesta alone but also among its family members. Early dynamical studies have suggested the existence of a Vesta dynamical family (Williams, 1979; Zappalá et al., 1990). Follow-up spectroscopic observations at visible wavelengths have confirmed the existence of such a family, revealing 20 small (diameters <10 kilometers) main-belt asteroids with optical reflectance spectral features similar to those of Vesta and eucrite and diogenite meteorites (Binzel & Xu, 1993). Since then, more than 15,000 objects have been identified as likely Vesta family members (Nesvorny, 2015), and several of these candidates have been confirmed via spectroscopic observations (e.g., Hardersen et al., 2014, 2015; Fulvio et al., 2018). We recall here that the term "Vestoid" is usually employed to designate a member of the Vesta family in the literature. Whereas the Vestoids are all located in Vesta's vicinity, between 2.1 and 2.5 AU, some V-types (see Tholen & Barucci, 1989; Bus & Binzel, 2002; DeMeo et al., 2009 for

https://doi.org/10.1017/9781108856324.003 Published online by Cambridge University Press

a definition of asteroid taxonomies) have also been discovered in the near-Earth space (Cruikshank et al., 1991; Binzel et al., 2004, 2019; Thomas et al., 2014) as well as in the middle and the outer belt (e.g., Lazzaro et al., 2000; Roig & Gil-Hutton, 2006; Moskovitz et al., 2008; Roig et al., 2008; Hardersen et al., 2018). Whereas V-type NEAs might have originated in the Vesta family and escaped the inner belt via the ν_6 and 3:1 resonances, it is unlikely to be the case for most middle and outer Main Belt V-types (e.g., Fulvio et al., 2018; Hardersen et al., 2018). (1459) Magnya, in particular, located at 3.15 AU, is unlikely to be from Vesta (Lazzaro et al., 2000; Hardersen et al., 2004). These results imply that the basaltic population present in the asteroid belt is not limited to Vesta and its family. Rather, it encompasses a larger number of bodies.

1.2.2 Extra-Terrestrial Analogues of D > 100 km Main Belt Asteroids

1.2.2.1 Asteroid Types with Plausible Meteoritic Analogues

Meteorites, which are mostly fragments of Main Belt asteroids, have played a key role in our understanding of the surface composition of asteroids and their distribution across the Main Belt. Their spectral properties have been measured in laboratories over an extended wavelength range (from the visible to the mid-infrared; e.g. Gaffey, 1976; Cloutis et al., 2010, 2011, 2012, 2013; Beck et al., 2014) and used for direct comparison with those acquired for asteroids via telescopic observations (see Burbine, 2014, 2016; DeMeo et al., 2015; Reddy et al., 2015; Vernazza & Beck, 2017, and references therein). Because most minerals present in meteorites possess diagnostic features either in the near- or mid-infrared and because quality measurements in these ranges became available for a large number of asteroids in the late 1990s, we can say that the Golden Age of asteroid compositional studies really started toward the end of the second millennium.

About 60% of the spectral types defined by DeMeo et al. (2009) (A, Cgh, Ch, K, Q, R, S, Sa, Sq, Sr, Sv, V, and some X, Xc, and Xk types) can be linked to (or entirely defined by) a given meteorite class. Hereafter, we make a brief summary of these associations as well as a review of the spectroscopic observations of D > 100 km bodies belonging to these classes:

- A-type asteroids mostly comprise the parent bodies of differentiated meteorites such as brachinites and pallasites, and possibly those of the undifferentiated R chondrite meteorites (Sunshine et al., 2007). (354) Eleonora is the only D > 100 km A-type asteroid and it contains more than 80% of the mass of all A-type bodies (DeMeo et al., 2019). Its composition is compatible with that of differentiated meteorites (Sunshine et al., 2007).
- Ch- and Cgh-type asteroids comprise the parent bodies of CM chondrites (Vilas & Gaffey, 1989; Vernazza et al., 2016, and references therein). The Main Belt contains 61 CM-like bodies with diameters greater than 100 km. The analysis of the visible and near-infrared spectral properties of 34 of these bodies were reported by Vernazza et al. (2016). They showed that the spectral variation observed among these bodies is essentially due to variations in the average regolith grain size. In addition, they showed that the spectral properties of the vast majority (unheated) of CM chondrites resemble both the surfaces and the interiors of CM-like bodies, implying a "low" temperature (<300°C) thermal evolution of the CM parent body(ies). It follows that an impact origin is the likely explanation for the existence of heated CM chondrites.
- K-type asteroids comprise the parent bodies of CV, CO, CR, and CK meteorites (e.g. Bell, 1988; Burbine et al., 2001; Clark et al., 2009). The four D > 100 km K-type asteroids are (9) Mertis, (42) Isis, (114) Kassandra, and (221) Eos, with Eos being the largest remnant of a large outer Main Belt family (e.g., Broz et al., 2013).
- The R-type class counts only one object so far, (349) Dembowska. Of interest to the present chapter, this object is a D > 100 km body and its meteoritic analogues may comprise both the lodranite and acapulcoite achondritic meteorites. While (349) Dembowska's visible and near infrared spectrum appear very similar to those of H-like S-type asteroids (Vernazza et al., 2015a), the depth of its 1- and 2-μm bands is much larger than that observed in S-type spectra (see Figure 1.1). As noticed by Vernazza et al. (2015a), both lodranites and acapulcoites have spectral properties and ol/(ol + low Ca-px) ratios that are very similar to those of ordinary chondrites and H chondrites in particular. Yet, given their lower iron content, the depth of their 1- and 2-μm bands are larger than those of H chondrites (see Figure 1.1), making them plausible analogues for a body such as (349) Dembowska.
- S-complex asteroids (Q, S, Sa, Sq, Sr, Sv) comprise the parent bodies of the most common type of meteorites, namely ordinary chondrites (~80% of the falls; see Vernazza et al., 2015b for a detailed review on this topic), and also possibly those of some differentiated meteorites such as lodranites and acapulcoites (Vernazza et al., 2015b). Vernazza et al. (2014) analyzed the visible and near-infrared spectral properties of nearly 100 S-type asteroids among which 23 bodies have diameters greater than 100 km (out of 24 in total). They found that the surface composition of these bodies is compatible with that of H, L, and LL ordinary chondrites, and that H-like bodies are located on average further from the sun than LL-like ones. This is somewhat counterintuitive given that H chondrites are more reduced than LL chondrites, suggesting a formation closer to the sun.
- (4) Vesta is the only D > 100 km V-type, and its connection with HED meteorites has been described in Section 1.2.1.
- X-complex asteroids (X, Xc, and Xk types) are representative of a great compositional diversity that largely exceeds (in terms of the number of compositional analogues) the number of taxonomic types. Their geometric albedos range from values below 0.05 to about 0.20. Notably, while some low albedo (<0.1) X-complex bodies likely comprise the parent bodies of rare types of meteorites such as Tagish Lake or CI chondrites, the remaining low albedo X-complex bodies appear unsampled by available meteorites in our collections (see Section 1.2.2.2). So far, there isn't a single D > 100 low albedo X-complex asteroid that can be unambiguously linked to either the Tagish Lake meteorite or CI chondrites. Concerning the high albedo (>0.1) X-complex bodies, they likely comprise the parent bodies of (1) iron meteorites (e.g. Cloutis et al., 1990; Shepard et al., 2015, and references therein), (2) enstatite chondrites (ECs) and aubrites (e.g., Vernazza et al., 2009, 2011; Ockert-Bell et al., 2010; Shepard et al., 2015), and (3) CB and CH chondrites (e.g., Hardersen et al., 2011; Shepard et al., 2015). The compositional interpretation of the visible and near-infrared spectral properties and/or the radar data for many D > 100 km

https://doi.org/10.1017/9781108856324.003 Published online by Cambridge University Press

X-complex asteroids can be found in Ockert-Bell et al. (2010), Hardersen et al. (2011), Vernazza et al. (2009, 2011), and Shepard et al. (2015).

1.2.2.2 Asteroid Types with No Clear Meteoritic Analogues

About 40% of the spectral types defined by DeMeo et al. (2009) (B, C, Cb, Cg, D, L, O, T, Xe, Xn, and most low albedo X, Xc, and Xk types) cannot be unambiguously linked to (or entirely defined by) a given meteorite class (e.g., Sunshine et al., 2008; Vernazza et al., 2015a, 2017).

In a few cases, this may be due to the rarity of the spectral type with L, O, Xe, and Xn types representing less than ∼1% of the mass of the Main Belt (DeMeo & Carry, 2013). As a matter of fact, our meteorite collections do certainly not sample every single Main Belt asteroid, and it may thus not be a surprise that some rare asteroid types are absent from our meteorite collections.

In most cases, however, the spectral mismatch between asteroid and meteorite spectra must be telling us something important about the nature of these unsampled yet abundant asteroid types (B, C, Cb, Cg, D, T, and low albedo X-, Xc-, and Xk-type asteroids represent at least 50% of the mass of the asteroid belt; DeMeo & Carry, 2013). Notably, these asteroid types (particularly the B, C, Cb, and Cg types) comprise – similarly to S-types – a high number of large asteroid families such as the Hygiea, Themis, Euphrosyne, Nemesis, and Polana-Eulalia (Pinilla-Alonso et al., 2016) families (see Broz et al., 2013 and Nesvorny, 2015 for further information on asteroid families). Considering that asteroid families are a major source of meteorites (this is well supported by the connection between the Vesta family and the HED meteorites), we should be receiving plenty of fragments from these bodies. Yet, this seems not to be the case, at least not under the form of consolidated meteorites. Note that metamorphosed CI/CM chondrites have been proposed in the past as analogues of B-, C-, Cb-, and Cg-type surfaces (Hiroi et al., 1993). However, such a possibility is presently untenable for the majority of these asteroids for three reasons, namely the paucity of these meteorites among falls (∼0.2% of meteorite falls) compared to the abundance of B-, C-, Cb,- and Cg-types and of families with similar spectral type, the difference in density between these meteorites and these asteroids (see Section 1.3.2), and the difference in spectral properties in the 3-μm region and in the mid-infrared region (e.g., Figure 1.2) between the two groups.

Vernazza et al. (2015a) proposed that these asteroid types might (at least their surfaces/outer shell) consist largely of friable materials unlikely to survive atmospheric entry as macroscopic bodies. It may thus not be surprising that these asteroid types are not well represented by the cohesive meteorites in our collections. Vernazza et al. (2015a) proposed that interplanetary dust particles (IDPs) as well as volatiles may, similarly to comets, be more appropriate analogues for these bodies. Available density measurements for these asteroid types ($\rho < 2$ g/cm^3 for $D > 200$ km bodies and in particular $\rho < 1.4$ g/cm^3 for the two largest low albedo X-type asteroids with $D > 250$ km; see Section 1.3.2) support such a hypothesis as they indicate that these bodies cannot be made of silicates only, and must comprise a significant fraction of ice(s). The discovery of several active objects among these asteroid types provides additional support for their comet-like nature (e.g., Hsieh & Jewitt, 2006; Jewitt, 2012; Jewitt et al., 2015). In addition, water ice may not only be present in the interior of these bodies but also at their surfaces (e.g., Campins et al., 2010; Rivkin & Emery, 2010; Licandro et al., 2011; Hargrove et al., 2012, 2015; Takir & Emery, 2012).

An analogy for these asteroid types with IDPs had already been proposed by Bradley et al. (1996) based on IDP spectra collected in the visible domain. In recent years, this association has been strengthened thanks to the availability of quality spectroscopic measurements for these asteroid types in the mid-infrared range (e.g., Barucci et al., 2002; Emery et al., 2006; Licandro et al., 2012; Marchis et al., 2012; Vernazza et al., 2013). Thanks to these datasets, it has been shown that the surfaces of some of these asteroid types (mainly low albedo X-, T-, and D-types and some C-types) are covered by a mixture of anhydrous amorphous and crystalline silicates (Vernazza et al., 2015a, 2017; Marsset et al., 2016), namely a composition that is similar to that of chondritic porous IDPs. Given that silicate grains in the interstellar medium (ISM) appear to be dominantly amorphous, these observations suggest a significant heritage from the ISM for these bodies. Furthermore, D-, low albedo X-, and T-type objects appear enriched in crystalline olivine with respect to pyroxene, whereas B-, C-, Cb-, and Cg-type asteroids tend to have about as much crystalline pyroxene as olivine (Vernazza et al., 2015a), suggesting two main primordial reservoirs of primitive small bodies as well as a compositional gradient in the primordial outer protoplanetary disk (10–40 AU).

Spectroscopic observations of these bodies in the so-called 3 μm region (which covers approximatively the 2.5–3.5 μm wavelength range; Rivkin et al., 2002, 2015) have allowed refining their surface compositions and thermal histories. In this wavelength region, all water-related materials (phyllosilicates including ammonium-bearing ones, water ice, brucite, to name a few) as well as absorbed water molecules in regolith particles (e.g., in lunar rocks or soils; Clark 2009) exhibit one or several absorption features. In the case of hydrated minerals, the absorption band is located at ∼2.7 to ∼2.8 μm (depending on the phyllosilicate mineralogy/hydration state), whereas in the case of water ice it is located at ∼3.05 μm. Hereafter, we summarize the findings of the two main spectroscopic surveys of $D > 100$ km asteroids in the 3-μm region:

- Takir and Emery (2012) and Takir et al. (2015) reported the observations of several tens of $D > 100$ km main-belt asteroids (mainly C-, low albedo X-, and T-types) with the NASA Infrared Telescope Facility (IRTF) located on the summit of Mauna Kea, Hawaii, and classified them into four spectral groups based on the absorption band centers and shapes ("sharp," "rounded," "Ceres-like," and "Europa-like"). The "sharp" group exhibits a characteristically sharp 3 μm feature attributed to hydrated minerals, whereas the "rounded" group exhibits a rounded 3 μm band attributed to H_2O ice. The "Ceres-like" group and "Europa-like" groups have narrow 3 μm band features centered at ∼3.05 μm and ∼3.15 μm, respectively. Whereas the "sharp" 3-μm feature appears similar to that observed in laboratory spectra of CM and CI chondrites and is mostly seen in the spectra of Ch- and Cgh-types, the other features are unlike those seen in meteorites (Rivkin et al., 2019). Whereas members of the "sharp," "Ceres-like," and "Europa-like" groups are concentrated in the 2.5–3.3 AU region, members of the "rounded" group are concentrated in the 3.4–4 AU region. Unlike the "sharp" group, the "rounded" group did not experience aqueous alteration (Takir & Emery, 2012).

https://doi.org/10.1017/9781108856324.003 Published online by Cambridge University Press

- The AKARI satellite made low-resolution spectroscopic observations in the 2.5–5 μm region with enough sensitivity to be able to characterize the surface composition of many D > 100 km Main Belt asteroids (Usui et al., 2019). AKARI observed 66 asteroids, including 23 C-complex asteroids, 22 X-complex asteroids, and 3 D-type asteroids. Most C-complex asteroids (17 out of 22; ∼77%), especially all CM-like bodies (Ch- and Cgh-types) and all B- and Cb-type asteroids, are found to possess a ∼2.7 μm feature associated with the presence of hydrated minerals at the surfaces of these objects, in agreement with Rivkin's (2012) results. Some C-complex asteroids such as (94) Aurora, however, do not show any obvious feature in the 3 μm band, suggesting an anhydrous surface composition. Most low-albedo X-complex (P-type) asteroids but only one D-type asteroid possesses an absorption feature at ∼2.7 μm, similarly suggesting the presence of hydrated minerals at their surfaces. For these objects, however, the depth of the ∼2.7 μm is shallower than that of C-type bodies, opening the possibility of a lower abundance of phyllosilicates at the surfaces of these bodies. It is interesting to notice that both the IRTF and AKARI surveys point to a compositional gradient among C-, P- (T- and low albedo X-), and D-type bodies, with C-complex bodies having the greatest abundance of phyllosilicates at their surfaces, followed by P-type bodies and finally D-type asteroids whose surfaces are mostly anhydrous. In addition, aqueously altered bodies are essentially concentrated inward of ∼3.3 AU, whereas dry ice-rich bodies are essentially concentrated outwards of ∼3.3 AU.

The presence of anhydrous silicates at the surface of some of these bodies implies they formed >5 Myrs after calcium–aluminum-rich inclusions (Neveu & Vernazza, 2019; Figure 1.3). Their anhydrous surface composition would otherwise have been lost due to melting and ice-rock differentiation driven by heating from the short-lived radionuclide ^{26}Al. It follows that IDP-like asteroids with anhydrous surfaces formed much later than the meteorite parent bodies, including CM-like bodies (Neveu & Vernazza, 2019; Figure 1.3).

In summary, IDPs (and volatiles) may reflect asteroid compositions at least as well as meteorites. A definitive confirmation of the link between IDPs and these asteroid classes will however require the acquisition of a consistent set of visible, near-infrared, and mid-infrared spectra (0.4–25 μm) for all classes of IDPs.

1.3 IMAGING OBSERVATIONS OF MAIN BELT ASTEROIDS

Whereas our understanding of the surface composition of asteroids and its distribution across the asteroid belt has improved enormously over the last decades (see Section 1.2) the same cannot be said regarding their internal structure, which is best characterized by the density. To constrain the density, one needs to fully reconstruct the 3D shape of a body to estimate its volume and to determine its mass from its gravitational interaction with other asteroids, or preferably, whenever possible, with its own satellite(s).

The lack of accurate density measurements for D > 100 km asteroids is due to the fact that disk-resolved observations of these bodies (which are needed to reconstruct their 3D shape) have until recently only been obtained with sufficient spatial resolution for a few bodies, either by dedicated interplanetary missions (e.g., Galileo, NEAR Shoemaker, Rosetta, Dawn, OSIRIS-REx, Hayabusa 1 & 2) or by remote imaging with the Hubble Space Telescope (HST), and adaptive-optics-equipped ground-based telescopes (e.g., VLT, Keck) in the case of the largest bodies (Vesta and Ceres).

The drastic increase in angular resolution provided by the new-generation adaptive-optics SPHERE/ZIMPOL instrument at the VLT with respect to the HST (about a factor of 3) implies that the largest Main Belt asteroids (with diameters greater than 100 km; angular size typically greater than 100 mas) become resolvable worlds and are thus no longer "extended point sources." With the SPHERE instrument, craters with diameters greater than approximately 30 km can now be recognized at the surfaces of

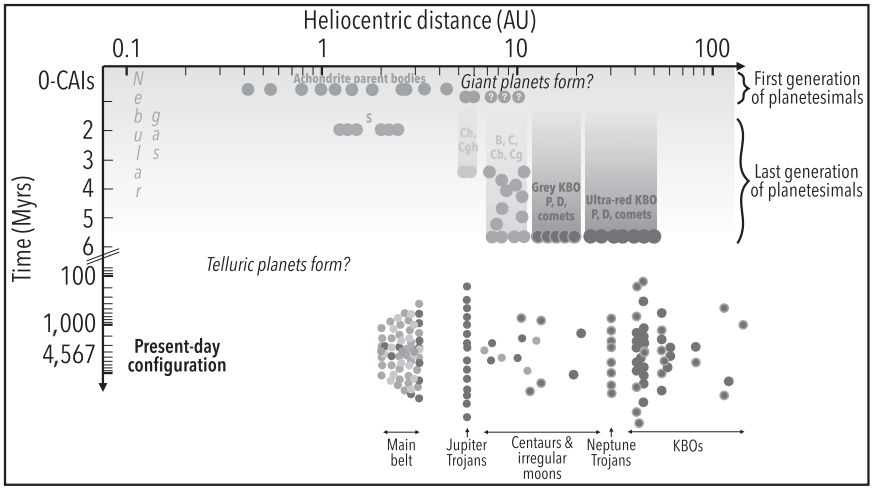

Figure 1.3 Postulated sequence of events tracing the time, place, and duration of formation of small bodies (top) to present-day observed characteristics (bottom; vertical spread reproducing roughly the distribution of orbital inclinations). The accretion duration is shown as gradient boxes ending at the fully formed bodies. Numerical simulations suggest that volatile-rich IDP-like bodies (blue dots; B, C, Cb, Cg, P, D, comets, grey and ultra-red KBOs) accreted their outer layers after 5–6 Myrs (adapted from Neveu & Vernazza, 2019).
A black and white version of this figure will appear in some formats. For the color version, refer to the plate section.

https://doi.org/10.1017/9781108856324.003 Published online by Cambridge University Press

Main Belt asteroids, and the shapes of the largest asteroids can be accurately reconstructed (e.g., Marsset et al., 2017).

In the present section, we first summarize the imaging observations of (1) Ceres and (4) Vesta performed from Earth prior to the arrival of the Dawn mission and further discuss how they compare to the Dawn observations. Second, we provide an overview of what is currently know regarding the shape, topography, and density of the largest Main Belt asteroids.

1.3.1 Focus on Earth-based Imaging Observations of Ceres and Vesta and Comparison to Dawn Measurements

1.3.1.1 (1) Ceres

Prior to the arrival of the Dawn mission in 2015, the highest resolution images of Ceres had been acquired with both the HST (Thomas et al., 2005) and the Keck II telescope on Mauna Kea (Carry et al., 2008), leading to a resolution at the surface of Ceres of the order of ~30 (HST) to ~50 (Keck) km.

Thomas et al. (2005) used the limb profiles of 217 HST images to constrain the shape and spin of Ceres. They found that the shape of Ceres can be well described by an oblate spheroid of semi-axes $a = b = 487.3 \pm 1.8$ km and $c = 454.7 \pm 1.6$ km (1σ), and a volume-equivalent radius of 476.2 ± 1.7 km. In addition, both the limb profiles and the tracking of Ceres' main bright spot (emplaced in what is known today as Occator crater) allowed constraining the spin to $291^\circ \pm 5^\circ$ (right ascension) and $59^\circ \pm 5^\circ$ (declination). The shape was further used to place constraints on Ceres' internal structure. First, it suggested that Ceres is a relaxed object in hydrostatic equilibrium. Second, using the determined density of 2.077 ± 0.036 g/cm^3 along with the a and c semi-axes, Thomas et al. (2005) concluded that Ceres is most likely a differentiated object. These HST images were further used by Li et al. (2006) to constrain Ceres' geometric and single-scattering albedos (respectively, 0.087 ± 0.003 and 0.070 ± 0.002 at 535 nm) and to produce the very first spatially resolved surface albedo maps of Ceres. The maps reveal a small albedo contrast (typically $< 4\%$ with respect to the average for most of the surface) with the bright spot being ~8% brighter than Ceres' average albedo.

Carry et al. (2008) performed a similar analysis using Keck/NIRC2 adaptive optics J/H/K imaging observations. Whereas they also found that Ceres' shape can be well described by that of an oblate spheroid, they derived different semi-axes values with respect to the HST results (Thomas et al., 2005), namely $a = b = 479.7 \pm 2.3$ km and $c = 444.4 \pm 2.1$ km (1σ), and a volume-equivalent radius of 467.6 ± 2.2 km, implying a ~5% higher density, namely 2.206 ± 0.043 g/cm^3. Concerning the internal structure, the Carry et al. (2008) study agreed with the findings by Thomas et al. (2005) that Ceres must be differentiated. Note that observations by Dawn imply that Ceres' interior is only partially differentiated (Park et al., 2016; Chapter 12). Finally, Carry et al. (2008) also constrained the spin axis to $288^\circ \pm 5^\circ$ (right ascension) and $66^\circ \pm 5^\circ$ (declination) and produced albedo maps in the different bands (J, H, K), revealing an albedo variegation similar to the one reported by Li et al. (2006).

Recently, Ceres has been imaged by the SPHERE instrument at the VLT revealing so far the most spectacular view of this object from Earth at a resolution of 4.4 km/pixel (Vernazza et al., 2020; Figure 1.4). A reflectance map based on the best-quality image (Vernazza et al., 2020) reveals a much higher albedo contrast (around ~20%) than previously reported (Li et al., 2006; Carry et al., 2008).

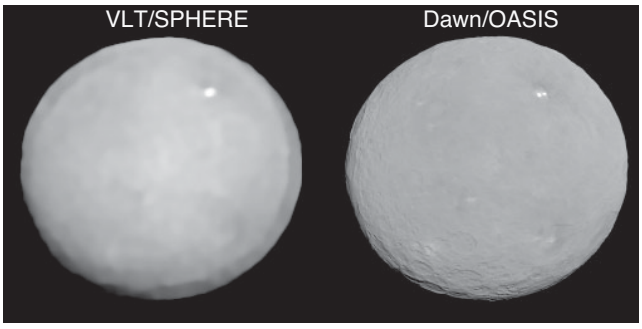

Figure 1.4 Comparison of the VLT/SPHERE deconvolved images of Ceres (left) with a synthetic projection of the Dawn 3D shape model produced with OASIS and with albedo information (right). The deconvolved image (left) shows a clear–dark–clear border, which is a deconvolution artefact.

When confronting Earth-based observations of Ceres with those of the NASA Dawn mission, it appears that the true dimensions of Ceres ($a = 483.1 \pm 0.2$ km, $b = 481.0 \pm 0.2$ km, and $c = 445.9 \pm 0.2$ km, and a volume-equivalent radius of 469.7 ± 0.2 km; Russell et al., 2016; Park et al., 2019) as well as its density (2.162 ± 0.003 g/cm^3; Russell et al., 2016) fall in between those determined early on by Thomas et al. (2005) and Carry et al. (2008) – although closer to those of Carry et al. (see Table 1.3). In addition, Ceres' exact pole coordinates (a right ascension of $291.43^\circ \pm 0.01^\circ$ and a declination of $66.76^\circ \pm 0.02^\circ$; Park et al., 2019) are very close to those derived earlier by Carry et al. (2008).

While the superior spatial resolution of the Dawn images has not drastically changed our knowledge of Ceres' dimensions and rotation axis, the same cannot be said regarding the surface topography and the variegation of the albedo across its surface. Schröder et al. (2017) have shown that Ceres' brightest spot corresponds to several extremely bright yet small areas within Occator crater, whose maximum size is ~10 km in diameter (Cerealia Facula) and whose average visual normal albedo is 0.6 ± 0.1, reaching locally a visual normal albedo close to unity at a scale of 35 m/pixel (see Chapter 10). The amplitude of the albedo variegation is thus much higher than that deduced from the SPHERE images considering that the average albedo is around 0.1.

Regarding the surface topography, Ceres possesses a heavily cratered surface with a paucity of large craters, suggesting that relaxation has occurred (Marchi et al., 2016). In contrast, craters can hardly be identified (at least not unambiguously) in the VLT/SPHERE images. This may be due to the morphology of $D > 30$ km craters (size limit above which craters can be resolved with VLT/SPHERE) as suggested by Vernazza et al. (2020). $D > 30$ km craters on Ceres are essentially flat floored, implying a smaller contrast between the crater floor and the crater rim than in the case of simple bowl shaped craters. Adding to that, a nonperfect correction of the atmospheric turbulence may lead to a global absence of contrast due to the topography in the deconvolved VLT/SPHERE images of Ceres. The same phenomenon is also observed in the case of other C-complex asteroids observed by VLT/SPHERE, such as (10) Hygiea (Vernazza et al., 2020) and (704) Interamnia (Hanus et al., 2020).

https://doi.org/10.1017/9781108856324.003 Published online by Cambridge University Press

Table 1.3 *Vesta and Ceres' physical and geological properties from Dawn compared to those derived from Earth.*

	Vesta (Earth-based)	Vesta (Dawn)	Ceres (Earth-based)	Ceres (Dawn)
Surface composition	HED meteorites (McCord et al., 1970)	- HED meteorites (De Sanctis et al., 2012) - Localized olivine-rich areas (Ammannito et al., 2013)	- Ammoniated phyllosilicates (King et al., 1992) - Carbonates (Rivkin et al., 2006b; Vernazza et al., 2017) - Brucite (Milliken & Rivkin, 2009)	- Mg- and NH_4-bearing phyllosilicates (De Sanctis et al., 2015; Ammannito et al., 2016) - Carbonates (De Sanctis et al., 2015, 2016) - Aliphatic organics (De Sanctis et al., 2017) - Localized water ice (Combe et al., 2016)
Meteorite analogue?	Yes (HEDs)	Yes (HEDs)	No	No
Volume equivalent radius	264.6 ± 5 km (Thomas et al., 1997a)	262.7 ± 0.1 km (Russell et al., 2012)	467.6 ± 2.2 km (Carry et al., 2008)	469.7 ± 0.1 km (Russell et al., 2016)
Dimensions	$(289 \times 280 \times 229) \pm 5$ km (Thomas et al., 1997a)	$(286.3 \times 278.6 \times 223.2) \pm 0.1$ km (Russell et al., 2012)	$(479.7 \times 479.7 \times 444.4) \pm 2.5$ km (Carry et al., 2008)	$(483.1 \times 481 \times 445.9) \pm 0.2$ km (Russell et al., 2016)
Spin axis	RA: $308^\circ \pm 10^\circ$ Dec: $48^\circ \pm 10^\circ$ (Thomas et al., 1997b)	RA: $309.03^\circ \pm 0.01^\circ$ Dec: $42.23^\circ \pm 0.01^\circ$ (Russell et al., 2012)	RA: $288^\circ \pm 5^\circ$ Dec: $66^\circ \pm 5^\circ$ (Carry et al., 2008)	RA: $291.42^\circ \pm 0.01^\circ$ Dec: $66.76^\circ \pm 0.02^\circ$ (Russell et al., 2016)
Mass	$2.6 \pm 0.3 \times 10^{20}$ kg (Konopliv et al., 2011)	$2.59076 \pm 0.00001 \times 10^{20}$ kg (Russell et al., 2012)	$9.31 \pm 0.06 \times 10^{20}$ kg (Konopliv et al., 2011)	$9.384 \pm 0.001 \times 10^{20}$ kg (Russell et al., 2016)

1.3.1.2 (4) Vesta

A few years after the discovery of the prominent Vesta family (Binzel & Xu, 1993), HST imaging observations of Vesta revealed the presence of an impact crater ~460 km in diameter near its south pole (Thomas et al., 1997a), thus strengthening the hypothesis of a collisional origin for Vesta-like bodies. The HST images were further used to constrain Vesta's spin, shape, and density, and to produce albedo, elevation, and compositional maps of its surface (Binzel et al., 1997; Thomas et al., 1997a, 1997b).

Thomas et al. (1997a) found that the shape of Vesta can be well described by a triaxial ellipsoid of semi-axes $a = 289 \pm 5$ km, $b = 280 \pm 5$ km, and $c = 229 \pm 5$ km, and a volume-equivalent radius of 264.6 ± 5 km. By combining the volume with the best mass estimates, they derived a mean density in the $3.5-3.9$ g/cm^3 range. In addition, the spin was constrained to $308^\circ \pm 10^\circ$ (right ascension) and $48^\circ \pm 10^\circ$ (declination) (Thomas et al., 1997b). The pole solution as well as the dimensions, including the volume-equivalent diameter, are very close to those derived from the Dawn imaging data (see Russell et al., 2012 and Table 1.3).

The HST images further revealed a strong albedo variegation across the surface (Binzel et al., 1997), as well as the presence of a prominent central peak within the impact basin whose height was estimated to be of the order of 13 km above the deepest part of the floor (Thomas et al., 1997a). The Dawn mission actually revealed the existence of two overlapping basins in the south polar region and a central peak whose height rivals that of Olympus Mons on Mars (e.g., Jaumann et al., 2012; Marchi et al., 2012; Russell et al., 2012; Schenk et al., 2012). The images of the Dawn mission also allowed the production of a high-resolution map of the albedo across Vesta's surface, revealing the second greatest variation of normal albedo of any asteroid yet observed after Ceres (the normal albedo varies between ~0.15 and ~0.6; Schröder et al., 2014; see also Chapter 6).

Recently, VLT/SPHERE images have recovered the surface of Vesta with a great amount of detail (Figure 1.5; Fetick et al., 2019). Most of the main topographic features present across Vesta's surface can be readily recognized from the ground. This includes the south pole impact basin and its prominent central peak, several $D \geq 25$ km sized craters, and also Matronalia Rupes, including its steep scarp and its small and big arcs. On the basis of these observations, it follows that next-generation telescopes with mirror sizes in the 30–40 m range (e.g., the Extremely Large Telescope, hereafter ELT) should in principle be able to resolve the remaining major topographic features of (4) Vesta (i.e., equatorial troughs, north–south crater dichotomy), provided that they operate at the diffraction limit in the visible range.

1.3.2 Overview of Earth-based Imaging Campaigns of Main Belt Asteroids

The large angular diameter of (1) Ceres and (4) Vesta at opposition (up to ~840 mas and ~700 mas, respectively) explains why these two bodies have been the subjects of in-depth studies using first-generation high angular resolution imaging systems such as HST

https://doi.org/10.1017/9781108856324.003 Published online by Cambridge University Press

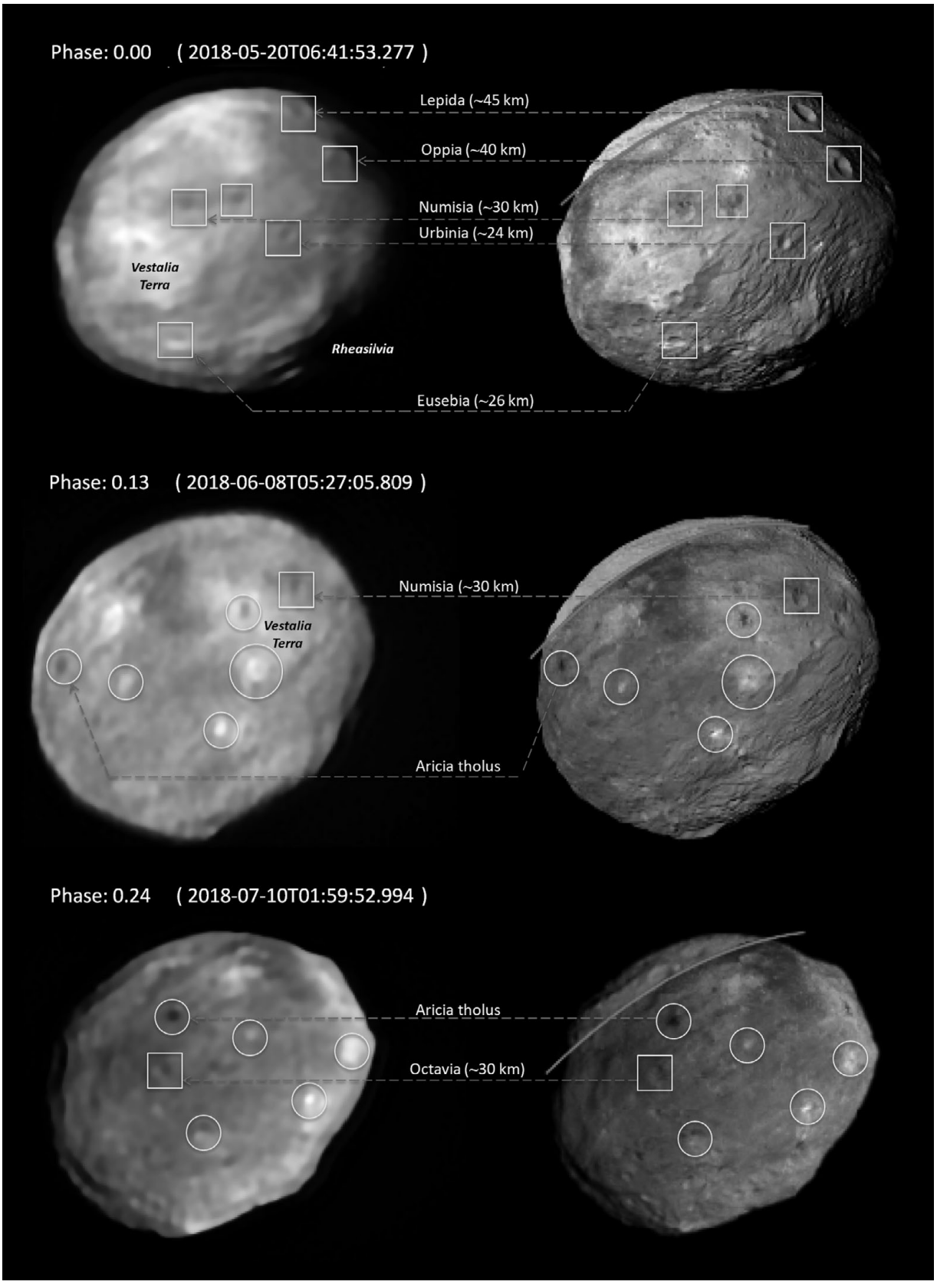

Figure 1.5 Comparison of the VLT/SPHERE deconvolved images of Vesta (left column) with synthetic projections of the Dawn 3D shape model produced with OASIS and with albedo information (right column). No albedo data is available from Dawn for latitudes above 30° N (orange line). The main structures that can be identified in both the VLT/SPHERE images and the synthetic ones are highlighted: craters are embedded in squares and albedo features in circles (from Fetick et al., 2019).
A black and white version of this figure will appear in some formats. For the color version, refer to the plate section.

https://doi.org/10.1017/9781108856324.003 Published online by Cambridge University Press

(resolution of ~50 mas). There are a few other Main Belt bodies that possess relatively large angular diameters at opposition ((2) Pallas: ~540 mas; (324) Bamberga: ~380 mas; (3) Juno, (7) Iris, and (10) Hygiea: ~325 mas) and that could have been valuable targets for dedicated observing campaigns using either HST or Keck/NIRC2. This has, however, only been the case for the largest of them ((2) Pallas; Schmidt et al., 2009; Carry et al., 2010a). Overall, before the advent of the SPHERE instrument at the VLT, sparse Keck/NIRC2 imaging data had been collected for many D > 100 km asteroids. Furthermore, these data were rarely acquired when the targets were at opposition, leading to non-optimal resolution for the observations of these bodies (Hanus et al., 2017b). Hereafter, we describe some important constraints that have been collected for D > 100 km asteroids based on high angular resolution imaging observations.

1.3.2.1 Asteroid Densities and Internal Structures

Density is the physical property that constrains best the interior of asteroids. Unfortunately, the latter has only been measured for a handful of asteroids (mostly in the case of multiple asteroids but also via in-situ space missions). Importantly, most D < 100 km asteroids are seen as collisionally evolved objects (Morbidelli et al., 2009) whose internal structure can be largely occupied by voids (called macroporosity, reaching up to 50–60% in some cases; Carry, 2012; Scheeres et al., 2015), thus limiting our capability to interpret meaningfully their bulk density in terms of composition(s). On the contrary, large bodies (D > 100 km) are seen as primordial remnants of the early Solar System (Morbidelli et al., 2009); that is their internal structure has likely remained intact since their formation (they can be seen as the smallest protoplanets). For most of these objects, the macroporosity is likely minimal (<20%) and their bulk density is therefore an excellent tracer of their bulk composition.

Following the discovery by the Galileo spacecraft of the first Main Belt asteroid's satellite (Dactyl, around (243) Ida; Chapman et al., 1995; Belton et al., 1995), high angular resolution imaging observations of the largest Main Belt asteroids were performed during the subsequent ~15 years to search for the presence of moons/companions. Note that accurate 3D shape reconstruction algorithms based on AO data such as KOALA (Carry et al., 2010b) and ADAM (Viikinkoski et al., 2015a) were not available during that time frame, leaving the moon search and the subsequent characterization of its orbit as the most compelling science objective. Indeed, direct imaging observations of multiple-asteroid systems are the most efficient approach from Earth for deriving precise asteroid masses. Specifically, the images provide constraints on the orbital parameters of the moon(s) and hence the total mass of the system. In the case of (a) small companion(s), the total mass is dominated by the primary implying that the mass of the primary can be well constrained (usually with a <10% uncertainty). The only other way to constrain masses of large asteroids with similar precision is via dedicated interplanetary missions, either a fly-by for the largest ones (as in the case of (21) Lutetia) or a rendezvous (e.g. Dawn mission, OSIRIS-REx, Hayabusa 1 & 2). Note that the orbital properties of the moon(s) can be used to constrain the dynamical quadrupole J_2; by comparing the latter with the J_2 derived from the 3D shape of the primary, one can search for the presence or absence of a mass concentration within the primary, hence a differentiated internal structure (e.g., Pajuelo et al., 2018).

At the time of writing the Asteroid III book, seven multiple systems were known among the largest (D > 90 km) Main Belt asteroids (Merline et al., 2002), and this number increased by a factor of two at the time of writing the Asteroid IV book (Margot et al., 2015). Since then, only one multiple system has been discovered among large Main Belt asteroids ((31) Euphrosyne and its moon; see Vernazza et al., 2019). Among these 15 multiple systems, six are triple systems, the first to be discovered being the one of (87) Sylvia (Marchis et al., 2005). Two thirds of these multiple systems belong to the C-complex, while the remaining systems belong either to the P or M classes. Surprisingly, there are currently no large S-types with known companions. Whereas the observed S/C type dichotomy may be interpreted as a consequence of compositional differences (hence different material strengths) implying a different response to impacts between the water-poor silicate-rich S-types and the water-rich C-types, the existence of the metal/silicate-rich Kalliope and Kleopatra systems complicates the picture.

Hereafter, we summarize current knowledge regarding the bulk composition of the main taxonomic classes (Figure 1.6). In the case of the largest S-type asteroids, the derived densities are consistent with those of ordinary chondrites (Viikinkoski et al., 2015b; Hanus et al., 2017b, 2019; Marsset et al., 2017), implying – contrary to asteroid (4) Vesta – an absence of large-scale differentiation for these bodies, which is in agreement with the thermal history of ordinary chondrites (Huss et al., 2006; Monnereau et al., 2013). Similarly, the density of the largest CM-like bodies (Cg/Cgh types) is consistent with that of CM chondrites, suggesting a homogeneous internal structure for these bodies (Carry et al., 2019). Concerning the remaining large (D > 200 km) C-complex bodies (C, Cb, Cg, and most B-types apart from Pallas), their density is in the 1.4–2.0 g/cm^3 range (Marchis et al., 2012; Hanus et al., 2020; Vernazza et al., 2020), implying a high water fraction for these bodies. Modeling results by Beauvalet and Marchis (2014) in the case of (45) Eugenia further suggest the presence of a denser core, possibly consistent with an early differentiation. A differentiated interior has also been advocated in the case of the largest C-type, (1) Ceres (e.g., Thomas et al., 2005; Park et al., 2016; Chapter 12). It is too early to conclude that all large water-rich C-types underwent differentiation, yet thermal evolution models suggest that such a trend was quasi unavoidable for D > 200 km objects consisting initially of a 70% rock, 30% ice composition by mass (Neveu & Vernazza, 2019). Finally, large P-type asteroids for which precise density estimates are available indicate a density in the 1.0–1.3 g/cm^3 range that appears substantially lower than that of water-rich C-types. It is worth mentioning that, for the two largest bodies – (87) Sylvia and (107) Camilla – the presence of a small dense core is predicted (Pajuelo et al., 2018, Carry et al., 2021). It is presently unclear whether these bodies are more water-rich than C-types or if they formed with substantial porosity (70–75%), as observed in the case of comet 67P/Churyumov-Gerasimenko (Jorda et al., 2016).

1.3.2.2 Asteroid Shapes

Because of their large masses, Solar System bodies with diameters larger than ~900 km possess rounded, ellipsoidal shapes, consistent with hydrostatic equilibrium, which is a part of the current IAU definition of a planet or a dwarf planet. On the other side of the

https://doi.org/10.1017/9781108856324.003 Published online by Cambridge University Press

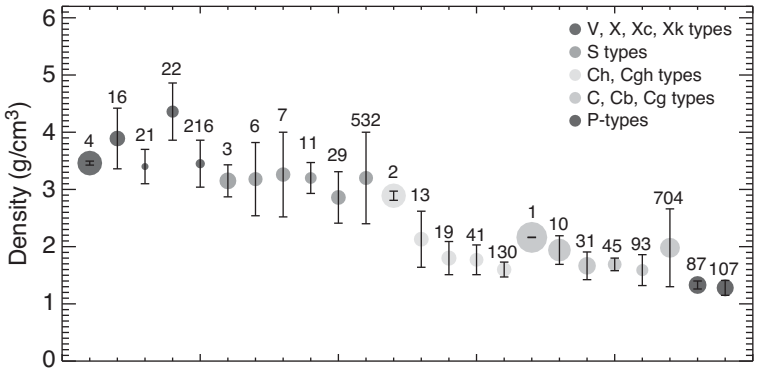

Figure 1.6 Density of some of the largest asteroids. Asteroids are grouped following their spectral classification. The relative sizes of the dots follow the relative diameters of the bodies in logarithmic scale. Error bars are 1-sigma. The science based on these density estimates can be retrieved in Paetzold et al. 2011, Russell et al. 2012, 2016, Viikinkoski et al. 2015b, Marsset et al. 2017, Hanus et al. 2017a, b, Pajuelo et al. 2018, Carry et al. 2019a, b, Ferrais et al. 2020, Hanus et al. 2020, Marsset et al. 2020, Vernazza et al. 2020, Vernazza et al. 2021, Yang et al. 2020 and Dudzinski et al. 2020.
A black and white version of this figure will appear in some formats. For the color version, refer to the plate section.

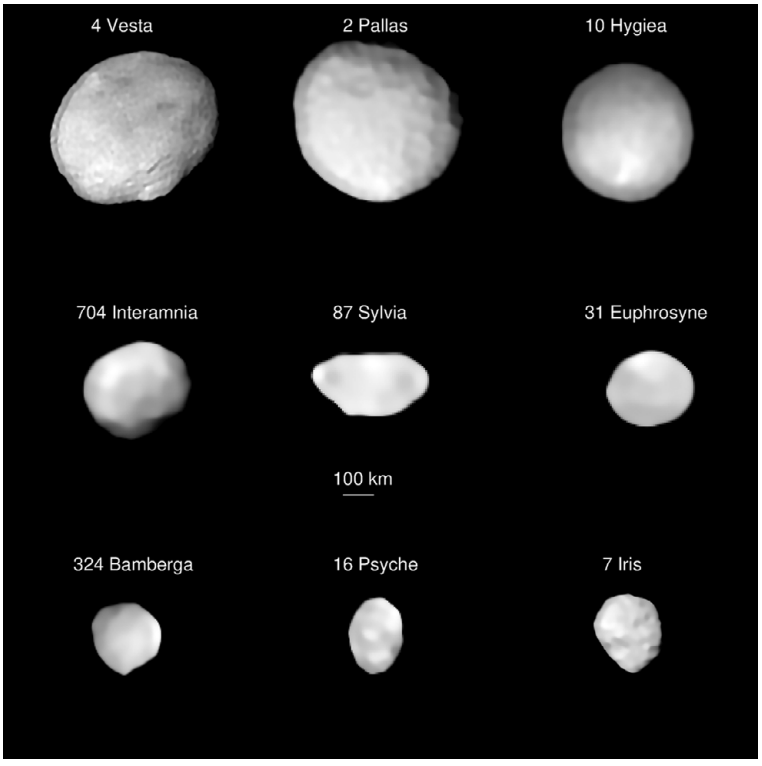

Figure 1.7 VLT/SPHERE images deconvolved with the MISTRAL algorithm (Fusco et al., 2003) of a sample of D > 200 km asteroids. The relative sizes are respected, and the scale is indicated on the plot. The objects appear according to decreasing values of their volume equivalent diameter (see Table 1.1). The science based on these images can be retrieved from Fetick et al. (2019), Hanus et al. (2019, 2020), Ferrais et al. (2020), Marsset et al. (2020), Vernazza et al. (2020), Yang et al. (2020) and Carry et al. (2021).

mass range, very small bodies (diameters < 100 km) tend to possess highly irregular shapes, with the notable exception of some D < 5 km bodies that are affected by the so-called YORP effect (Yarkovsky–O'Keefe–Radzievskii–Paddack; Rubincam, 2000; Vokrouhlický et al., 2003), and which have similar shapes to a spinning top (e.g., Ryugu, or Bennu; Nolan et al., 2013; Watanabe et al., 2019). However, it remains to be tested at what size range the shape of a typical minor body transits from a nearly rounded equilibrium shape to an irregular shape and to what extent this size range depends on factors such as the bulk composition of the minor planet or its collisional and thermal history (Hanus et al., 2020).

Recently, an imaging survey of a substantial fraction of all D > 100 km Main Belt asteroids (sampling the main compositional classes) has been conducted using VLT/SPHERE (Vernazza et al., 2018, 2020; Viikinkoski et al., 2018; Carry et al., 2019; Fetick et al., 2019; Hanus et al., 2019, 2020; Ferrais et al., 2020; Marsset et al., 2020; Yang et al., 2020; Figure 1.7). So far, it appears that water-rich asteroids with D > 250 km have shapes close to

https://doi.org/10.1017/9781108856324.003 Published online by Cambridge University Press

equilibrium (Ferrais et al., 2020; Yang et al., 2020). At similar sizes, rocky bodies such as (3) Juno appear more irregular. Still, rocky or even metal-rich bodies such as Psyche with D > 200 km have shapes that are closer to that of an ellipsoid than D < 200 km bodies (Ferrais et al., 2020), suggesting that the transition from a regular equilibrium shape to a fully irregular shape is smooth. The equilibrium shapes of water-rich bodies suggest that these bodies were fluid during their history, either as the result of early thermal heating leading to aqueous alteration of their interiors or because of large impacts and subsequent reaccumulation (e.g., Vernazza et al., 2020; Yang et al., 2020).

1.3.2.3 Cratering History of D > 100 km Asteroids

Prior to the first light of the adaptive-optics SPHERE imaging system at ESO/VLT in 2014, the characterization of the surface topography of asteroids had only been performed via dedicated in situ space missions (Galileo, NEAR Shoemaker, Hayabusa 1&2, Rosetta, Dawn, OSIRIS-REx) with the notable exception of Vesta's south pole impact basin detected by HST (Thomas et al., 1997a). The SPHERE survey of D > 100 km asteroids (Vernazza et al., 2018) has drastically augmented the number of asteroid craters detected from Earth. For example, Fetick et al. (2019) detected nine craters larger than 25 km in diameter on Vesta (e.g., Figure 1.5), Hanus et al. (2019) identified eight impact craters 20–40 km in diameter on (7) Iris, while Marsset et al. (2020) identified 36 craters larger than 30 km in diameter on (2) Pallas. The large number of D > 30 km craters on Pallas appears to be consistent with its high inclination (∼35°) implying a more violent collisional history than that of Vesta or Ceres. Also, VLT/SPHERE observations of asteroid (89) Julia (Vernazza et al., 2018), a D ∼ 140 km S-type asteroid and the parent body of a small collisional family that consists of 66 known members with D < 2.5 km, have revealed the presence of an impact crater (∼75 km wide) that could be the origin of this family. These results highlight the fact that the geological history of asteroids can now be investigated from the ground for a large number of asteroids, thus nicely complementing higher resolution data obtained in situ for a few bodies.

1.4 CONCLUSION AND PERSPECTIVE

When confronting the measurements of the global physical properties (average surface composition, size, shape, spin, rotation period, density) obtained from Earth with those obtained in-situ for both Vesta and Ceres, it appears that the results are about the same within errors (Table 1.3). This underlines the reliability of Earth-based observations and of the methods employed to analyze the data, especially when they are collected from the ground requiring atmospheric correction. Notably, recent VLT/SPHERE imaging observations have demonstrated in a striking manner how the gap between interplanetary missions and ground-based observations is getting narrower (Fetick et al., 2019; Vernazza et al., 2020). With the advent of extremely large telescopes (ELT, GMT, TMT), the science objectives of future interplanetary missions to Main Belt asteroids will have to be carefully thought out so that these missions will complement – not duplicate – what will be achieved via Earth-based telescopic observations. For instance, future ELT adaptive-optics imaging of main-belt asteroids will allow us to resolve craters down to ∼5 km in size, implying that we shall be able to characterize their global geological history from the ground. This implies that geological and geomorphological studies (based on high angular resolution imaging data) might become – during the coming decade – the prime science objectives that will be conducted from Earth in the case of large D > 100 km asteroids, dethroning studies related to the nature/origin of these bodies (deduced from the analysis of their spectra). Interplanetary missions to Main Belt asteroids performing cosmochemistry experiments, landing, and eventually a sample return should be preferred at the forefront of *in-situ* exploration as these would ideally complement the investigations conducted from Earth. In particular, IDP-like asteroids as well as the rare L-, Xe-, Xn- and O-types should be preferred targets as little is known regarding these bodies due to the paucity/absence of samples for these objects in our collections.

REFERENCES

A'Hearn, M. F., & Feldman, P. D. (1992) Water vaporization on Ceres. *Icarus*, 98, 54–60.

Allen, D. A. (1970) Infrared diameter of Vesta. *Nature*, 227, 158–159.

Ammannito, E., DeSanctis, M. C., Ciarniello, M., et al. (2016) Distribution of phyllosilicates on the surface of Ceres. *Science*, 353.

Ammannito, E., DeSanctis, M. C., Palomba, E., et al. (2013) Olivine in an unexpected location on Vesta's surface. *Nature* 504, 122–125.

Barucci, M. A., Dotto, E., Brucato J., et al. (2002) 10 Hygiea: ISO infrared observations. *Icarus*, 156, 202–210.

Beauvalet, L., & Marchis, F. (2014) Multiple asteroid systems (45) Eugenia and (87) Sylvia: Sensitivity to external and internal perturbations. *Icarus*, 241, 13–25.

Beck, P., Garenne, A., Quirico, E., et al. (2014) Transmission infrared spectra (2–25 μm) of carbonaceous chondrites (CI, CM, CV-CK, CR, C2 ungrouped): Mineralogy, water, and asteroidal processes. *Icarus*, 229, 263–277.

Bell, J. F. (1988) A probable asteroidal parent body for the CV or CO chondrites (abstract). *Meteoritics*, 23, 256–257.

Belton, M. J. S., Chapman C. R., Thomas, P. C., et al. (1995) Bulk density of asteroid 243 Ida from the orbit of its satellite Dactyl. *Nature*, 374, 785–788.

Binzel, R. P., DeMeo, F. E., Turtelboom, E. V., et al. (2019) Compositional distributions and evolutionary processes for the near-Earth object population: Results from the MIT-Hawaii Near-Earth Object Spectroscopic Survey (MITHNEOS). *Icarus*, 324, 41–76.

Binzel, R. P., Gaffey, M. J., Thomas, P. C., et al. (1997) Geologic mapping of Vesta from 1994 Hubble Space Telescope images. *Icarus*, 128, 95–103.

Binzel, R. P., Rivkin, A. S., Stuart, J., et al. (2004) Observed spectral properties of near-Earth objects: Results for population distribution, source regions, and space weathering processes. *Icarus*, 170, 259–294.

Binzel, R. P., & Xu, S. (1993) Chips off of asteroid 4 Vesta: Evidence for the parent body of basaltic achondrite meteorites. *Science*, 260, 186–191.

Blanco, C., & Catalano, S. (1979) UBV photometry of Vesta. *Icarus*, 40, 359–363.

Bottke, W. F., Nesvorny, D., Grimm, R. E., Morbidelli, A., & O'Brien, D. P. (2006) Iron meteorites as remnants of planetesimals formed in the terrestrial planet region. *Nature*, 439, 821–824.

Bowell, E., & Zellner, B. (1973) Polarizations of asteroids and satellites. In T. Gehrels (ed.), *Planets, Stars and Nebulae Studied with Photopolarimetry*. Tucson: University of Arizona Press, pp. 381–403.

Bradley, J. P., Keller, L. P., Brownlee, D. E., & Thomas, K. L. (1996). Reflectance spectroscopy of interplanetary dust particles. *Meteoritics and Planetary Science*, 31, 394–402.

Broz, M., Morbidelli, A., Bottke, W. F., et al. (2013) Constraining the cometary flux through the asteroid belt during the late heavy bombardment. *Astronomy & Astrophysics*, 551, A117.

Brunetto, R., Borg, J., Dartois, E., et al. (2011) Mid-IR, Far-IR, Raman micro-spectroscopy, and FESEM-EDX study of IDP L2021C5: Clues to its origin. *Icarus*, 212, 896–910.

Burbine, T. H. (2014) *Asteroids. Planets, Asteriods, Comets and The Solar System, Volume 2 of Treatise on Geochemistry*, 2nd ed., ed. Andrew M. Davis. Amsterdam: Elsevier, pp. 365–415.

Burbine, T. H. (2016) Advances in determining asteroid chemistries and mineralogies. *Chemie der Erde – Geochemistry*, 76, 181–195.

Burbine, T. H., Binzel, R. P., Bus, S. J., & Clark, B. E. (2001). K asteroids and CO3/CV3 chondrites. *Meteoritics & Planetary Science*, 36, 245–253.

Bus, S. J., & Binzel, R. P. (2002) Phase II of the small main-belt asteroid spectroscopic survey: A feature-based taxonomy. *Icarus*, 158, 146–177.

Campins, H., Hargrove, K., Pinilla-Alonson, N., *et al*. (2010) Water ice and organics on the surface of the asteroid 24 Themis. *Nature*, 464, 1320–1321.

Carry, B. (2012) Density of asteroids. *Planetary and Space Science*, 73, 98–118.

Carry, B., Dumas, C., Fulchignoni, M., et al. (2008) Near-infrared mapping and physical properties of the dwarf-planet Ceres. *Astronomy and Astrophysics*, 478, 235–244.

Carry, B., Dumas, C., Kaasalainen, M., et al. (2010a) Physical properties of (2) Pallas. *Icarus*, 205, 460–472.

Carry, B., Kaasalainen, M., Leyrat, C., et al. (2010b) Physical properties of the ESA Rosetta target asteroid (21) Lutetia. II. Shape and flyby geometry. *Astronomy and Astrophysics*, 523, A94.

Carry, B., Vachier, F., Berthier, J., et al. (2019) Homogeneous internal structure of CM-like asteroid (41) Daphne. *Astronomy and Astrophysics*, 623, A132.

Carry, B., Vernazza, P., Vachier, F., et al. (2021) Evidence of differentiation of the most primitive small bodies. *Astronomy and Astrophysics*, 630, A129.

Carry, B., Vernazza, P., Dumas, C., & Fulchignoni, M. (2010c) First disk-resolved spectroscopy of (4) Vesta. *Icarus*, 205, 473–482.

Chapman, C. R., McCord, T. B., & Johnson, T. V. (1973) Asteroid spectral reflectivities. *The Astronomical Journal*, 78, 126–140.

Chapman, C. R., Morrison, D., Zellner, B. (1975) Surface properties of asteroids: A synthesis of polarimetry, radiometry, and spectrophotometry. *Icarus*, 24, 104–130.

Chapman, C. R., Veverka, J., Thomas, P. C., et al. (1995) Discovery and physical properties of Dactyl, a satellite of asteroid 243 Ida. *Nature*, 374, 783–785.

Clark, B. E., Ockert-Bell, M. E., Cloutis, E. A., et al. (2009) Spectroscopy of K-complex asteroids: Parent bodies of carbonaceous meteorites? *Icarus*, 202, 119–133.

Clark, R. N. (2009) Detection of adsorbed water and hydroxyl on the moon. *Science*, 326, 562–564.

Cloutis, E. A., Gaffey, M. J., Smith, D. G. W., & Lambert, R. St. J. (1990) Reflectance spectra of "featureless" materials and the surface mineralogies of M- and E-class asteroids. *Journal of Geophysical Research*, 95, 281–293.

Cloutis, E. A., Hardensen, P. S., Bish, D. L., et al. (2010) Reflectance spectra of iron meteorites: Implications for spectral identification of their parent bodies. *Meteoritics and Planetary Science*, 45, 304–332.

Cloutis, E. A., Hiroi, T., Gaffey, M. J., Alexander, C. M. O'D., & Mann, P. (2011) Spectral reflectance properties of carbonaceous chondrites: 1. CI chondrites. *Icarus*, 212, 180–209.

Cloutis, E. A., Hudon, P., Hiroi, T., & Gaffey, M. J. (2012) Spectral reflectance properties of carbonaceous chondrites 4: Aqueously altered and thermally metamorphosed meteorites. *Icarus*, 220, 586–617.

Cloutis, E. A., Izawa, M. R. M., Pompilio, L., et al. (2013). Spectral reflectance properties of HED meteorites + CM2 carbonaceous chondrites: Comparison to HED grain size and compositional variations and implications for the nature of low-albedo features on Asteroid 4 Vesta. *Icarus*, 223, 850–877.

Combe, J.-Ph., McCord, T. B., Tosi, F., et al. (2016) Detection of local H_2O exposed at the surface of Ceres. *Science*, 353, aaf3010.

Cruikshank, D. P., & Morrison, D. (1973). Radii and albedos of asteroids 1, 2, 3, 4, 6, 15, 51, 433, and 511. *Icarus*, 20, 477–481.

Cruikshank, D. P., Tholen, D. J., Hartmann, W. K., Bell, J. F., & Brown, R. H. (1991) Three basaltic earth-approaching asteroids and the source of the basaltic meteorites. *Icarus*, 89, 1–13.

De Sanctis, M. C., Ammannito, E., Capria, M. T., et al. (2012) Spectroscopic characterization of mineralogy and its diversity across Vesta. *Science*, 336, 697–700.

De Sanctis, M. C., Ammannito, E., McSween, H. Y., et al. (2017) Localized aliphatic organic material on the surface of Ceres. *Science*, 355, 719–722.

De Sanctis, M. C., Ammannito, E., Raponi, A., et al. (2015) Ammoniated phyllosilicates with a likely outer Solar System origin on (1) Ceres. *Nature*, 528, 241–244.

De Sanctis, M. C., Ammannito, E., Raponi, A., et al. (2020) Fresh emplacement of hydrated sodium chloride on Ceres from ascending salty fluids. *Nature Astronomy*, 4, 786–793.

De Sanctis, M. C., Raponi, A., Ammannito, E., et al. (2016) Bright carbonate deposits as evidence of aqueous alteration on (1) Ceres. *Nature*, 536, 54–57.

Degewij, J., Tedesco, E. F., & Zellner, B. (1979) Albedo and color contrasts on asteroid surfaces. *Icarus*, 40, 364–374.

DeMeo, F. E., Alexander, C. M. O., Walsh, K. J., Chapman, C. R., & Binzel, R. P. (2015) The compositional structure of the asteroid belt. In P. Michel, F. E. DeMeo, & W. F. Bottke (eds.), *Asteroids IV*. Tucson: University of Arizona Press, pp. 13–42.

DeMeo, F. E., Binzel, R. P., Slivan, S. M., & Bus, S. J. (2009) An extension of the Bus asteroid taxonomy into the near-infrared. *Icarus*, 202, 160–180.

DeMeo, F. E., & Carry, B. (2013) The taxonomic distribution of asteroids from multi-filter all sky photometric surveys. *Icarus*, 226, 723–741.

DeMeo, F. E., & Carry, B. (2014) Solar System evolution from compositional mapping of the asteroid belt. *Nature*, 505, 629–634.

DeMeo, F. E., Polihook, D., Carry, B., et al. (2019) Olivine-dominated A-type asteroids in the Main Belt: Distribution, abundance and relation to families. *Icarus*, 322, 13–30.

Dotto, E., Müller, T. G., Barucci, M. A., et al. (2000) ISO results on bright Main Belt asteroids: PHT-S observations. *Astronomy and Astrophysics*, 358, 1133–1141.

Drake, M. J. (2001) The eucrite/Vesta story. *Meteoritics & Planetary Science*, 36, 501–513.

Emery, J. P., Cruikshank, D. P., & van Cleve, J. (2006) Thermal emission spectroscopy (5.2–38 μm) of three Trojan asteroids with the Spitzer Space Telescope: Detection of fine-grained silicates. *Icarus*, 182, 496–512.

Feierberg, M. A., & Drake, M. J. (1980) The meteorite–asteroid connection: The infrared spectra of Eucrites, Shergottites, and Vesta. *Science*, 209, 805–807.

Feierberg, M. A., Larson, H. P., Fink, U., & Smith, H. A. (1980) Spectroscopic evidence for two achondrite parent bodies: asteroids 349 Dembowska and 4 Vesta. *Geochimica et Cosmochimica Acta*, 44, 513–524.

Ferrais, M., Vernazza, P., Jorda, L., et al. (2020) Asteroid (16) Psyche's primordial shape: A possible Jacobi ellipsoid, *Astronomy & Astrophysics*, 638, L15.

Fetick, R., Jorda, L., Vernazza, P., et al. (2019) Closing the gap between Earth-based and interplanetary mission observations: Vesta seen by VLT/SPHERE. *Astronomy & Astrophysics*, 623, A6.

Fulvio, D., Ieva, S., Perna, D., et al. (2018) Statistical analysis of the spectral properties of V-type asteroids: A review on what we known and what is still missing. *Planetary and Space Science*, 164, 37–43.

Fusco, T., Mugnier, L. M., Conan, J.-M., et al. (2003) Deconvolution of astronomical images obtained from ground-based telescopes with adaptive optics. In P. L. Wizinowich, & D. Bonaccini (eds.), *Adaptive Optical System Technologies II. Proceedings of the SPIE 4839*. Bellingham, WA: SPIE, pp. 1065–1075.

Gaffey, M. J. (1976) Spectral reflectance characteristics of the meteorite classes. *Journal of Geophysical Research*, 81, 905–920.

Gaffey, M. J. (1997) Surface lithologic heterogeneity of asteroid 4 Vesta. *Icarus*, 127, 130–157.

Gomes, R., Levison, H. F., Tsiganis, K., & Morbidelli, A. (2005) Origin of the cataclysmic late heavy bombardment period of the terrestrial planets. *Nature*, 435, 466–469.

Gradie, J., & Tedesco, E. (1982) Compositional structure of the asteroid belt. *Science*, 216, 1405–1407.

Greenwood, R. C., Burbine, T. H., & Franchi, I. A. (2020) Linking asteroids and meteorites to the primordial planetesimal population. Geochimica. *Et Cosmochimica Acta*, 27, 377–406.

Hanus, J., Marchis, F., Viikinkoski, M., et al. (2017a) Shape model of asteroid (130) Elektra from optical photometry and disk-resolved images from VLT/SPHERE and Nirc2/Keck. *Astronomy & Astrophysics*, 599, A36.

Hanus, J., Marsset, M., Vernazza, P., et al. (2019) The shape of (7) Iris as evidence of an ancient large impact ? *Astronomy & Astrophysics*, 624, A121.

Hanus, J., Vernazza, P., Viikinkoski, M., et al. (2020) (704) Interamnia: A transitional object between a dwarf planet and a typical irregular-shaped minor body. *Astronomy & Astrophysics*, 633, A65.

Hanus, J., Viikinkoski, M., Marchis, F., et al. (2017b) Volumes and bulk densities of forty asteroids from ADAM shape modeling. *Astronomy & Astrophysics*, 601, A114.

Hardersen, P., Cloutis, E., Reddy, V., et al. (2011) The M-/X-asteroid menagerie: Results of an NIR spectral survey of 45 main-belt asteroids. *Meteoritics & Planetary Science*, 46, 1910–1938.

Hardersen, P., Gaffey, M. J., & Abel, P. A. (2004) Mineralogy of Asteroid 1459 Magnya and implications for its origin. *Icarus*, 167, 170–177.

Hardersen, P., Reddy, V., Cloutis, E., et al. (2018) Basalt or not? Near-infrared spectra, surface mineralogical estimates, and meteorite analogs for 33 Vp-type asteroid. *The Astronomical Journal*, 156, 11.

Hardersen, P., Reddy, V., & Roberts, R. (2015) Vestoids, part II: The Basaltic nature and HED meteorite analogs for eight Vp-type asteroids and their associations with (4) Vesta. *The Astrophysical Journal Supplement Series*, 221, 19.

Hardersen, P., Reddy, V., Roberts, R., & Mainzer, A. (2014) More chips off of asteroid (4) Vesta: Characterization of eight Vestoids and their HED meteorite analogs. *Icarus*, 242, 269–282.

Hargrove, K. D., Emery, J. P., Campins, H., & Kelley, M. S. (2015) Asteroid (90) antiope: Another icy member of the Themis family? *Icarus*, 254, 150–156.

Hargrove, K. D., Kelley, M. S., Campins, H., et al. (2012) Asteroids (65) cybele, (107) Camilla and (121) Hermione: Infrared spectral diversity among the cybeles. *Icarus*, 221, 453–455.

Hasegawa, S., Kuroda, D., Yanagisawa, K., & Usui, F. (2017) Follow-up observations for the asteroid catalog using AKARI spectroscopic observations. *Publications of the Astronomical Society of Japan*, 69, 99.

Hasegawa, S., Miyasaka, S., Tokimasa, N., et al. (2014) The opposition effect of the asteroid 4 Vesta. *Publications of the Astronomical Society of Japan*, 66, 89.

Hasegawa, S., Murakawa, K., Ishiguro, M., et al. (2003) Evidence of hydrated and/or hydroxylated minerals on the surface of asteroid 4 Vesta. *Geophysical Research Letters*, 30, 2123.

Heras, A. M., Morris, P. W., Vandenbussche, B., & Müller, T. G. (2000) Asteroid 4 Vesta as seen with the ISO short wavelength spectrometer. In M. L. Sitko, A. L. Sprague, & O. K. Lynch (eds.), *Thermal Emission Spectroscopy and Analysis of Dust, Disks and Regoliths, Astronomical Society of the Pacific Conference Series*, 196. San Francisco, CA: ASP, pp. 205–213.

Hiroi, T., Pieters, C. M., & Takeda, H. (1994) Grain size of the surface regolith asteroid 4 Vesta estimated from its reflectance spectrum in comparison with HED meteorites. *Meteoritics*, 29, 394–396.

Hiroi, T., Pieters, C. M., Zolensky, M. E., & Lipschutz, M. E. (1993) Evidence of thermal metamorphism on the C, G, B, and F asteroids. *Science*, 261, 1016–1018.

Hsieh, H. H., & Jewitt, D. A. (2006) Population of comets in the main asteroid belt. *Science*, 312, 561–563.

Huss, G. R., Rubin, A. E., & Grossman, J. N. (2006) Thermal metamorphism in chondrites. In D. S. Lauretta, & H. Y. McSween Jr. (eds.), *Meteorites and the Early Solar System II*. Tucson: University of Arizona Press, pp. 567–586.

Jaumann, R., Williams, D. A., Buczkowski, D. L., et al. (2012) Vesta's shape and morphology. *Science*, 336, 687–690.

Jewitt, D. (2012). The active asteroids. *The Astronomical Journal*, 143, 66.

Jewitt, D., Hsieh, H. H., & Agaral, J. (2015) The active asteroids. In P. Michel, F. E. DeMeo, & W. F. Bottke (eds.), *Asteroids IV*. Tucson: University of Arizona Press, pp. 221–242.

Johnson, T. V., & Fanale, F. P. (1973) Optical properties of carbonaceous chondrites and their relationship to asteroids. *Journal of Geophysical Research*, 78, 8507–8518.

Johnson, T. V., Matson, D. L., Veeder, G. J., & Loer, S. J. (1975) Asteroids: Infrared photometry at 1.25, 1.65, and 2.2 microns. *Astrophysical Journal*, 197, 527–531.

Jorda, L., Gaskell, R., Capanna, C., et al. (2016) The global shape, density and rotation of Comet 67P/Churyumov-Gerasimenko from preperihelion Rosetta/OSIRIS observations. *Icarus*, 277, 257–278.

King, T. V. V., Clark, R. N., Calvin, W. M., Sherman, D. M., & Brown, R. H. (1992) Evidence for ammonium-bearing minerals on Ceres. *Science*, 255, 1551–1553.

Konopliv, A. S., Asmar, S. W., Folkner, W. M., et al. (2011) Mars high resolution gravity fields from MRO, Mars seasonal gravity, and other dynamical parameters. *Icarus*, 211, 401–428.

Larson, H. P., & Fink, U. (1975) Infrared spectral observations of asteroid 4 Vesta. *Icarus*, 26, 420–427.

Lazzaro, D., Angeli, C. A., Carvano, J. M., et al. (2004) S^3OS^2: The visible spectroscopic survey of 820 asteroids. *Icarus*, 172, 179–220.

Lazzaro, D., Michtchenko, T., Carvano, J. M., et al. (2000) Discovery of a basaltic asteroid in the outer Main Belt. *Science*, 288, 2033–2035.

Lebofsky, L. A. (1978) Asteroid 1 Ceres: Evidence for water of hydration. *Monthly Notices of the Royal Astronomical Society*, 182, 17–21.

Lebofsky, L. A., Feierberg, M. A., Tokunaga, A. T., et al. (1981) The 1.7 to 4.2 μm spectrum of asteroid 1 Ceres: Evidence for structural water in clay minerals. *Icarus*, 48, 453–459.

Levison, H. F., Bottke, W. F., Gounelle, M., *et al*. (2009) Contamination of the asteroid belt by primordial trans-Neptunian objects. *Nature*, 460, 364–366.

Li, J.-Y., McFadden, L., Parker, J., et al. (2006) Photometric analysis of 1 Ceres and surface mapping from HST observations. *Icarus*, 182, 143–160.

Licandro, J., Campins, H., Kelley, M., et al. (2011) (65) Cybele: Detection of small silicate grains, water-ice, and organics. *Astronomy and Astrophysics*, 525, id.A34.

Licandro, J., Hargrove, K., Kelley, M., *et al*. (2012) 5–14 μm Spitzer spectra of Themis family asteroids. *Astronomy and Astrophysics*, 537, A73.

Marchi, S., Ermakov, A. I., Raymond, C. A., et al. (2016) The missing large impact craters on Ceres. *Nature Communications*, 7, 12257.

Marchi, S., McSween, H. Y., O'Brien, D. P., et al. (2012) The violent collisional history of asteroid 4 Vesta. *Science*, 336, 690–694.

Marchis, F., Descamps, P., Hestroffer, D., & Berthier, J. (2005) Discovery of the triple asteroidal system 87 Sylvia. *Nature*, 436, 822–824.

Marchis, F., Enriquez, J. E., Emery, J. P., et al. (2012) Multiple asteroid systems: Dimensions and thermal properties from Spitzer Space Telescope and ground-based observations. *Icarus*, 221, 1130–1161.

Margot, J.-L., Pravec, P., Taylor, P., et al. (2015) Asteroid systems: Binaries, triples, and pairs. In P. Michel, F. E. DeMeo, & W. F. Bottke (eds.), *Asteroids IV*. Tucson: University of Arizona Press, pp. 355–374.

Marsset, M., Broz, M., Vernazza, P., et al. (2020) The violent collisional history of aqueously evolved (2) Pallas. *Nature Astronomy*, 4, 569–576.

Marsset, M., Carry, B., Dumas, C., et al. (2017) 3D shape of asteroid (6) Hebe from VLT/SPHERE imaging: Implications for the origin of ordinary H chondrites. *Astronomy & Astrophysics*, 604, A64.

Marsset, M., Vernazza, P., Birlan, M., et al. (2016) Compositional characterisation of the Themis family. *Astronomy & Astrophysics*, 586, A15.

Masiero, J. R., Grav, T., Mainzer, A. K., et al. (2014) Main-belt asteroids with WISE/NEOWISE: Near-infrared albedos. *The Astrophysical Journal*, 791, 121.

Masiero, J. R., Mainzer, A. K., Grav, T., et al. (2011) Main Belt asteroids with WISE/NEOWISE. I. Preliminary albedos and diameters. *The Astrophysical Journal*, 741, 68.

Matson, D. L. (1971) Infrared Emission from Asteroids at Wavelengths of 8.5, 10.5 and 11.6 Millimicron. PhD thesis, California Institute of Technology.

McCord, T., Adams, J., & Johnson, T. V. (1970) Asteroid Vesta: Spectral reflectivity and compositional implications. *Science*, 168, 1445–1447.

McFadden, L. A., McCord, T. B., & Pieters, C. (1977) Vesta: The first pyroxene band from new spectroscopic measurements. *Icarus*, 31, 439–446.

Merline, W. J., Weidenshilling, S. J., Durda, D. D., et al. (2002) Asteroids do have satellites. In W. F. Bottke Jr., A. Cellino, P. Paolicchi, & R. P. Binzel (eds.), *Asteroids III*, Tucson: University of Arizona Press, pp. 289–312.

Merouane, S., Djouadi, Z., & Le Sergeant d'Hendecourt, L. (2014) Relations between aliphatics and silicate components in 12 stratospheric particles deduced from vibrational spectroscopy. *The Astrophysical Journal*, 780, 174.

Milliken, R. E., & Rivkin, A. S. (2009) Brucite and carbonate assemblages from altered olivine-rich materials on Ceres. *Nature Geoscience*, 2, 258–261.

Monnereau, M., Toplis, M. J., Baratoux, D., & Guignard, J. (2013) Thermal history of the H-chondrite parent body: Implications for metamorphic grade and accretionary time-scale. *Geochimica et Cosmochimica Acta*, 119, 302–321.

Morbidelli, A., Bottke, W. F., Nesvorny, D., & Levison, H. F. (2009) Asteroids were born big. *Icarus*, 204, 558–573.

Morbidelli, A., Levison, H. F., Tsiganis, K., & Gomes, R. (2005) Chaotic capture of Jupiter's Trojan asteroids in the early Solar System. *Nature*, 435, 462–465.

Moskovitz, M., Jedicke, R., Gaidos, E., et al. (2008) The distribution of basaltic asteroids in the Main Belt. *Icarus*, 198, 77–90.

Nesvorny, D. (2015) *Nesvorny HCM Asteroid Families V3.0. EAR-A-VARGBDET-5-NESVORNYFAM-V3.0*. NASA Planetary Data System.

Neveu, M., & Vernazza, P. (2019) IDP-like asteroids formed later than 5 Myr after Ca-Al rich inclusions. *The Astrophysical Journal*, 875, 30.

Nolan, M. C., Magri, C., Howell, E. S., et al. (2013) Shape model and surface properties of the OSIRIS-REx target Asteroid (101955) Bennu from radar and lightcurve observations. *Icarus*, 226, 629–640.

Ockert-Bell, M. E., Clark, B. E., Shepard, M. K., et al. (2010) The composition of M-type asteroids: Synthesis of spectroscopic and radar observations. *Icarus*, 210, 674–692.

Pajuelo, M., Carry, B., Vachier, F., et al. (2018) Physical, spectral, and dynamical properties of asteroid (107) Camilla and its satellites. *Icarus*, 309, 134–161.

Park, R. S., Konopliv, A. S., Bills, B. G., et al. (2016) A partially differentiated interior for (1) Ceres deduced from its gravity field and shape. *Nature*, *537*, 515–517.

Park, R. S., Vaughan, A. T., Konopliv, A. S., et al. (2019) High-resolution shape model of Ceres from stereophotoclinometry using Dawn imaging data. *Icarus*, 319, 812–827.

Pinilla-Alonso, N., De Leon, J., Walsh, K. J., et al. (2016) Portrait of the Polana-Eulalia family complex: Surface homogeneity revealed from near-infrared spectroscopy. *Icarus*, 274, 231–248.

Raymond, S. N., & Izidoro, A. (2017) The empty primordial asteroid belt. *Science Advances*, 3, e1701138.

Reddy, V., Dunn, T. L., Thomas, C. A., Moskovitz, N. A., & Burbine, T. H. (2015) Mineralogy and surface composition of asteroids. In P. Michel, F. E. DeMeo, & W. F. Bottke (eds.), *Asteroids IV*. Tucson: University of Arizona Press, pp. 43–64.

Rivkin, A. S. (2012) The fraction of hydrated C-complex asteroids in the asteroid belt from SDSS data. *Icarus*, 221, 744–752.

Rivkin, A. S., Campins, H., Emery, J. P., et al. (2015) Astronomical observations of volatiles on asteroids. In P. Michel, F. E. DeMeo, & W. F. Bottke (eds.), *Asteroids IV*. Tucson: University of Arizona Press, pp. 65–87.

Rivkin, A. S., & Emery, J. P. (2010) Detection of ice and organics on an asteroidal surface. *Nature*, 464, 1322–1323.

Rivkin, A. S., Howell, E. S., & Emery, J. P. (2019) Infrared spectroscopy of large, low-albedo asteroids: Are Ceres and Themis archetypes or outliers? *Journal of Geophysical Research: Planets*, 124, 1393–1409.

Rivkin, A. S., Howell, E. S., Vilas, F., & Lebofsky, L. A. (2002) Hydrated minerals on asteroids: The astronomical record. In W. F. Bottke Jr., A. Cellino, P. Paolicchi, & R. P. Binzel (eds.), *Asteroids III*. Tucson: University of Arizona Press, pp. 235–253.

Rivkin, A. S., Li, J.-Y., Milliken, R. E., et al. (2011) The surface composition of Ceres. *Space Science Reviews*, 163, 95–116.

Rivkin, A. S., McFadden, L., Binzel, R. P., & Sykes, M. (2006a) Rotationally-resolved spectroscopy of Vesta I: 2 4 μm region. *Icarus*, 180, 464–472.

Rivkin, A. S., Volquardsen, E. L., & Clark, B. E. (2006b) The surface composition of Ceres: Discovery of carbonates and iron-rich clays. *Icarus*, 185, 563–567.

Roig, F., & Gil-Hutton, R. (2006) Selecting candidate V-type asteroids from the analysis of the Sloan Digital Sky Survey colors. *Icarus*, 183, 411–419.

Roig, F., Nesvorný, D., Gil-Hutton, R., & Lazzaro, D. (2008) V-type asteroids in the middle Main Belt. *Icarus*, 194, 125–136.

Rubincam, D. P. (2000) Radiative spin-up and spin-down of small asteroids. *Icarus*, 148, 2–11.

Russell, C. T., Raymond, C. A., Ammannito, E., et al. (2016) Dawn arrives at Ceres: Exploration of a small, volatile-rich world. *Science*, 353, 1008–1010.

Russell, C. T., Raymond, C. A., Coradini, A., et al. (2012) Dawn at Vesta: Testing the protoplanetary paradigm. *Science*, 336, 684–686.

Ryan, E. L., & Woodward, C. E. 2010. Rectified asteroid albedos and diameters from IRAS and MSX photometry catalogs. *The Astronomical Journal*, 140, 933–943.

Scheeres, D. J., Britt, D., Carry, B., & Holsapple, K. A. (2015) *Asteroid interiors and morphology*. In P. Michel, F. E. DeMeo, & W. F. Bottke (eds.), *Asteroids IV*. Tucson: University of Arizona Press, pp. 745–766.

Schenk, P., O'Brien, D. P., Marchi, S., et al. (2012) The geologically recent giant impact basins at Vesta's south pole. *Science*, 336, 694.

Schmidt, B. E., Thomas, P. C., Bauer, J. M., et al. (2009) The shape and surface variation of 2 Pallas from the Hubble space telescope. *Science*, 326, 275–278.

Schröder, S. E., Mottola, S., Carsenty, U., et al. (2017) Resolved spectrophotometric properties of the Ceres surface from Dawn Framing Camera images. *Icarus*, 288, 201–225.

Schröder, S. E., Mottola, S., Keller, H. U., et al. (2014) Resolved spectrophotometric properties of the Ceres surface from Dawn Framing Camera images. *Planetary and Space Science*, 103, 66–81.

Shepard, M. K., Taylor, P. A., Nolan, M. C., et al. (2015) A radar survey of M- and X-class asteroids. III. Insights into their composition, hydration state, and structure. *Icarus*, 245, 38–55.

Sunshine, J. M., Bus, S. J., Corrigan, C. M., McCoy, T. J., & Burbine, T. H. (2007) Olivine-dominated asteroids and meteorites: Distinguishing nebular and igneous histories. *Meteoritics & Planetary Science*, 42, 155–170.

Sunshine, J. M., Connolly, H. C., McCoy, T. J., et al. (2008) Ancient asteroids enriched in refractory inclusions. *Science*, 320, 514–516.

Takir, D., & Emery, J. P. (2012) Outer Main Belt asteroids: Identification and distribution of four 3-mum spectral groups. *Icarus*, 219, 641–654.

Takir, D., Emery, J. P., & McSween, H. Y. (2015) Toward an understanding of phyllosilicate mineralogy in the outer main asteroid belt. *Icarus*, 257, 185–193.

Tedesco, E. F., Noah, P. V., Noah, M., & Price, S. D. (2002) The supplemental IRAS minor planet survey. *The Astronomical Journal*, 123, 1056–1085.

Tholen, D. J., & Barucci, M. A. (1989) Asteroid taxonomy. In R. P. Binzel, T. Gehrels, & M. S. Matthews (eds.), *Asteroids II*. Tucson: University of Arizona Press, pp. 298–315.

Thomas C. A., Emery J. P., Trilling D. E., et al. (2014) Physical characterization of warm Spitzer-observed near-Earth objects. *Icarus*, 228, 217–246.

Thomas, P. C., Binzel. R. P., Gaffey, M. J., et al. (1997a) Impact excavation on asteroid 4 Vesta: Hubble space telescope results. *Science*, 277, 1492–1495.

Thomas, P. C., Binzel. R. P., Gaffey, M. J., et al. (1997b) Vesta: Spin pole, size, and shape from HST images. *Icarus*, 128, 88–94.

Thomas, P. C., Parker, J. Wm., McFadden, L., et al. (2005) Differentiation of the asteroid Ceres as revealed by its shape. *Nature*, 437, 224–226.

Tsiganis, K., Gomes, R., Morbidelli, A., & Levison, H. F. (2005) Origin of the orbital architecture of the giant planets of the Solar System. *Nature*, 435, 459–461.

Usui, F., Hasegawa, S., Ootsubo, T., & Onaka, T. (2019) AKARI/IRC near-infrared asteroid spectroscopic survey: AcuA-spec. *Publications of the Astronomical Society of Japan*, 71, 1.

Usui, F., Kuroda, D. Müller, T. G., et al. (2011) Asteroid catalog using AKARI: AKARI/IRC mid-infrared asteroid survey. *Publications of the Astronomical Society of Japan*, 63, 1117–1138.

Vernazza, P., & Beck, P. (2017) Composition of Solar System small bodies. In L. T. Elkins-Tanton, & B. P. Weiss (eds.), *Planetesimals: Early Differentiation and Consequences for Planets*. Cambridge: Cambridge University Press, pp. 269–297.

Vernazza, P., Broz, M., Drouard, D., et al. (2018) The impact crater at the origin of the Julia family detected with VLT/SPHERE? *Astronomy & Astrophysics*, 618, A154.

Vernazza, P., Brunetto, R., Binzel, R. P., et al. (2009) Plausible parent bodies for enstatite chondrites and mesosiderites: Implications for Lutetia's fly-by. *Icarus*, 202, 477–486.

Vernazza, P., Carry, B., Vachier, F., et al. (2019) New satellite around (31) Euphrosyne. *IAU circular 4627*.

Vernazza, P., Castillo-Rogez, J., Beck, P., et al. (2017) Different origins or different evolutions? Decoding the spectral diversity among C-type asteroids. *The Astrophysical Journal*, 153, 72.

Vernazza, P., Ferrais, M., Jorda, L., et al. VLT/SPHERE imaging survey of the largest main-belt asteroids: Final results and synthesis. A&A 654, A56, 2021.

Vernazza, P., Fulvio, D., Brunetto, R., et al. (2013) Paucity of Tagish Lake-like parent bodies in the asteroid belt and among Jupiter trojans. *Icarus*, 225, 517–525.

Vernazza, P., Jorda, L., Sevecek, P., et al. (2020) A basin-free spherical shape as an outcome of a giant impact on asteroid Hygiea. *Nature Astronomy*, 4, 136–141.

Vernazza, P., Lamy, P., Groussin, O., et al. (2011) Asteroid (21) Lutetia as a remnant of Earth's precursor planetesimals. *Icarus*, 216, 650–659.

Vernazza, P., Marsset, B., Beck, P., et al. (2015a) Interplanetary dust particles as samples of icy asteroids. *The Astrophysical Journal*, 806, 204.

Vernazza, P., Marsset, B., Beck, P., et al. (2016) Compositional homogeneity of CM parent bodies. *The Astrophysical Journal*, 152, 54.

Vernazza, P., Mothé-Diniz, T., Barucci, M. A., et al. (2005) Analysis of near-IR spectra of 1 Ceres and 4 Vesta, targets of the Dawn mission. *Astronomy & Astrophysics*, 436, 1113–1121.

Vernazza, P., Zanda, B., Binzel, R. P., et al. (2014) Multiple and fast: The accretion of ordinary chondrite parent bodies. *Astrophysical Journal*, 791, 120.

Vernazza, P., Zanda, B., Nakamura, T., et al. (2015b) The formation and evolution of ordinary chondrite parent bodies. In P. Michel, F. E. DeMeo, & W. F. Bottke (eds.), *Asteroids IV*. Tucson: University of Arizona Press, pp. 617–634.

Veverka, J. F. (1970) Photometric and Polarimetric Studies of Minor Planets and Satellites. PhD thesis, Harvard University.

Viikinkoski, M., Kaasalainen, M., & Durech, J. (2015a) ADAM: A general method for using various data types in asteroid reconstruction. *Astronomy & Astrophysics*, 576, A8.

Viikinkoski, M., Kaasalainen, M., Durech, J., et al. (2015b) VLT/SPHERE- and ALMA-based shape reconstruction of asteroid (3) Juno. *Astronomy & Astrophysics*, 581, L3.

Viikinkoski, M., Vernazza, P., Hanus, J., et al. (2018) (16) Psyche: A mesosiderite-like asteroid? *Astronomy & Astrophysics*, 619, L3.

Vilas, F., & Gaffey, M. J. (1989) Phyllosilicate absorption features in main-belt and outer-belt asteroid reflectance spectra. *Science*, 246, 790–792.

Vokrouhlický, D., Nesvorný, D., & Bottke, W. F. (2003) The vector alignments of asteroid spins by thermal torques. *Nature*, 425, 147–151.

Walsh, K. J., Morbidelli, A., Raymond, S. N., O'Brien, D. P., & Mandell, A. M. (2011) A low mass for Mars from Jupiter's early gas-driven migration. *Nature*, 475, 206–209.

Watanabe, S., HiraBayashi, M., Hirata, N., et al. (2019) Hayabusa2 arrives at the carbonaceous asteroid 162173 Ryugu – A spinning top-shaped rubble pile. *Science*, 364, 268–272.

Williams, J. G. (1979) Proper elements and family memberships of the asteroids. In T. Gehrels (ed.), *Asteroids*. Tucson: University of Arizona Press, pp. 1040–1063.

Yang, B., Hanus, J, Carry, B., et al. (2020) Binary asteroid (31) Euphrosyne: Ice-rich and nearly spherical. *Astronomy & Astrophysics*, 641, A80.

Yang, B., & Jewitt, D. (2010) Identification of magnetite in B-type asteroids. *The Astronomical Journal*, 140, 692–698.

Zappalà, V., Cellino, A., Farinella, P., & Knežević, Z. (1990) Asteroid families. I. Identification by hierarchical clustering and reliability assessment. *The Astronomical Journal*, 100, 2030–2046.